JGR Solid Earth

RESEARCH ARTICLE
10.1029/2019JB017352

Dynamic Probabilistic Hazard Mapping in the Long Valley Volcanic Region CA: Integrating Vent Opening Maps and Statistical Surrogates of Physical Models of Pyroclastic Density Currents

Regis Rutarindwa[1], Elaine T. Spiller[1], Andrea Bevilacqua[2,3,4], Marcus I. Bursik[2], and Abani K. Patra[3,5]

[1]Department of Mathematical and Statistical Sciences, Marquette University, Milwaukee, WI, USA, [2]Department of Earth Sciences, State University of New York, Buffalo, NY, USA, [3]Computational Data Sciences and Engineering Program, State University of New York, Buffalo, NY, USA, [4]Istituto Nazionale di Geofisica e Vulcanologia, Pisa, Italy, [5]Department of Mechanical Engineering, State University of New York, Buffalo, NY, USA

Key Points:
- Statistical emulators of computationally intensive physical models enable rapid assessment of hazard threats due to volcanic avalanches
- Probabilistic hazard maps allow one to visualize the probability of hazard threat under different probabilistic scenario models
- Impacts of aleatoric and epistemic uncertainties in vent opening models on volcanic hazards can be quantified in probabilistic hazard maps

Supporting Information:
- Data Set S1
- Supporting Information S1

Correspondence to:
E. T. Spiller,
elaine.spiller@marquette.edu

Citation:
Rutarindwa, R., Spiller, E. T., Bevilacqua, A., Bursik, M. I., & Patra, A. K. (2019). Dynamic probabilistic hazard mapping in the Long Valley Volcanic Region CA: Integrating vent opening maps and statistical surrogates of physical models of pyroclastic density currents. *Journal of Geophysical Research: Solid Earth*, *124*. https://doi.org/10.1029/2019JB017352

Received 11 JAN 2019
Accepted 10 AUG 2019
Accepted article online 16 AUG 2019

Abstract Ideally, probabilistic hazard assessments combine available knowledge about physical mechanisms of the hazard, data on past hazards, and any precursor information. Systematically assessing the probability of rare, yet catastrophic hazards adds a layer of difficulty due to limited observation data. Via computer models, one can exercise potentially dangerous scenarios that may not have happened in the past but are probabilistically consistent with the aleatoric nature of previous volcanic behavior in the record. Traditional Monte Carlo-based methods to calculate such hazard probabilities suffer from two issues: they are computationally expensive, and they are static. In light of new information, newly available data, signs of unrest, and new probabilistic analysis describing uncertainty about scenarios the Monte Carlo calculation would need to be redone under the same computational constraints. Here we present an alternative approach utilizing statistical emulators that provide an efficient way to overcome the computational bottleneck of typical Monte Carlo approaches. Moreover, this approach is independent of an aleatoric scenario model and yet can be applied rapidly to any scenario model making it dynamic. We present and apply this emulator-based approach to create multiple probabilistic hazard maps for inundation of pyroclastic density currents in the Long Valley Volcanic Region. Further, we illustrate how this approach enables an exploration of the impact of epistemic uncertainties on these probabilistic hazard forecasts. Particularly, we focus on the uncertainty of vent opening models and how that uncertainty both aleatoric and epistemic impacts the resulting probabilistic hazard maps of pyroclastic density current inundation.

Plain Language Summary We present a method to forecast the probability of inundation by hot volcanic flows of rock and gas. In some sense, we can think of a natural hazard forecast much like a weather forecast. Instead of *how likely is it to rain tomorrow*, we might ask *how likely is our town or the nearby power plant to get inundated by a volcanic flow?* The weather forecasting analogy is, however, flawed in an important way when dealing with rare events. Large-scale, highly destructive volcanic flows are rare events, of course, and it is human nature to think that such events will happen as they have in the past. But often the scale (here think mass of the flowing material) varies randomly, and sometimes an event bigger in scale than any in the historical recorded will happen. Thus, to generate hazard forecasts, we must rely on a combination of models—models of the physics governing the volcanic flows as well as models that describe the probabilistic nature of historical data. Unfortunately, the typical process of combining these models would require thousands of hours on a super computer. Instead, we build a surrogate model of the physical volcanic flow model that alleviates the computational bottleneck.

1. Introduction/Motivation

Mapping of volcanic hazards is often based on field reconstructions and numerical modeling of specific past events. In contrast, our goal is to produce dynamic *probabilistic* hazard maps—maps of probabilities

indicating the likelihood of a hazard affecting the mapped locations—that are consistent with past events but can reflect both aleatory uncertainty inherent in the system and epistemic uncertainty due to imperfect models and limited data (Marzocchi & Bebbington, 2012; Sparks, 2003). Further, a single probabilistic forecast map is not the goal—instead, we wish to see how dynamic probabilistic hazard maps change as we explore these uncertainties (Bevilacqua, Neri, et al., 2017; Neri et al., 2015). Ultimately, we envision these dynamic probabilistic hazard maps as a tool to explore the impacts of uncertainties on probabilistic hazard forecasts for those charged with making a hazard map. This paper provides an efficient and reliable statistical framework to analyze hazards under uncertainty.

Physical simulations of pyroclastic density currents (PDCs), such as those employed in TITAN2D (Patra et al., 2005), are indispensable for examining the possible impact of PDCs for a wide range of potential scenarios *where, how large*, and *how frequent*. Such scenarios need to be characterized to provide initial and boundary conditions at which PDC simulations are exercised. That said, characterizing potential scenarios is a significant scientific task in its own right. The inherent (aleatoric) randomness of such scenarios demands a probabilistic description. The probabilistic hazard mapping tool outlined in this paper enables one to readily combine a probabilistic scenario model—inputs scenarios treated as random variables and modeled by probability density functions—with physical simulations to yield a probabilistic description of the hazard. Furthermore, this methodology is independent of any specific probabilistic scenario model and yet can rapidly produce a probabilistic hazard map once a probabilistic scenario model is chosen. This allows one to compare probabilistic hazard maps under several probabilistic scenario models and to quickly update a hazard map as new data or more sophisticated probabilistic scenario models become available.

Probabilistic assessments of volcanic hazards based on simulations of physical processes have gained traction over the past several years (Bevilacqua et al., 2019; Biass, Bonadonna, Di Traglia, et al., 2016; Biass, Bonadonna, Connor, et al., 2016; Cappello et al., 2015; Connor et al., 2012; Dalbey et al., 2008; Gallant et al., 2018; Mastin et al., 2014; Mead & Magill, 2017; Sandri et al., 2016, 2018; Tierz et al., 2018; Volentik & Houghton, 2015). Computer model emulators (also known as statistical surrogates) are an efficient tool in this type of modeling particularly when the physical model is computationally expensive to exercise (Bayarri et al., 2009, 2015; Spiller et al., 2014). Probabilistic approaches are particularly useful as they let one explore the impact of "tail events" in a systematic fashion. In other words, via simulation, one can exercise potentially dangerous scenarios that may not have happened in the recent past but are probabilistically consistent with previous volcanic behavior. Typically, these strategies rely on Monte Carlo (MC) simulations to perform probability calculations (e.g., of a hazard inundation at a particular location), as the underlying question *does a particular sample scenario lead to inundation or not at the location of interest?* cannot be answered analytically. Standard MC integration is limited by the computational expense of physical simulations as it converges slowly, requiring typically $O(10^3–10^6)$ unique simulations.

The computational expense of standard MC does not readily allow us to change or update probabilistic scenario models. Neither does standard MC let us explore the impact of our models being imperfect nor our knowledge of the data being incomplete, for example, the impact of epistemic uncertainty on hazard forecasts. This is problematic. As states of activity in a hazard system evolve, likely so will our choice of probabilistic scenario models describing the aleatoric variability. Further, hazard assessments in volcanology are often characterized with a high degree of epistemic uncertainty. Ultimately, one hopes to model both aleatoric variability and epistemic uncertainty in a *doubly stochastic sense* in which a probability distribution reflecting aleatory variability of the system is itself uncertain (Bevilacqua et al., 2016; Marzocchi & Bebbington, 2012; Ogata & Akaike, 1982; Sparks & Aspinall, 2013). Indeed, for example, the initiation site of a hazardous flow can be modeled by an uncertain probability distribution (Bevilacqua et al., 2015; Bevilacqua, Bursik, et al., 2017; Selva et al., 2012; Tadini et al., 2017). The statistical tool described in this study avoids the computational roadblock of standard MC and as such can rapidly produce dynamic probabilistic hazard maps.

Utilizing *statistical surrogates* is a key innovation to overcoming the computational limitations of standard MC. Effectively, such emulators are a statistical model of physical models (Sacks et al., 1989, 2013; Welch et al., 1992). Statistical emulators can effectively replace a computationally expensive physical simulation with a computationally "free" function evaluation. Further, they allow one to account for any uncertainty introduced be replacing the simulator with the emulator.An emulator-based approach to probabilistic hazard mapping is "dynamic" in that it allows one to explore the impacts of various sources and varieties

of uncertainty—including estimates of the probability of vent opening as a function of location—more efficiently than ever before.

We developed this tool for the Long Valley volcanic region (LVVR) just east of the Sierra Nevada escarpment in California. Although some details of this approach are specific to Long Valley (aspects of the scenario space to focus on, digital elevation models, etc.), the general approach is not specific to a particular volcano or region. Further, we developed this tool for PDC hazards, but the tool hinges on a very general strategy of using surrogate models of physical simulations to identify important regions of input scenario space. In this sense, we anticipate that the approach presented here and variations thereof will prove useful for a wide range of volcanic hazards—lahars, tephra fallout, and pyroclastic surges. In particular, we imagine that such an approach could be useful to overcome computational challenges described in Biass, Bonadonna, Di Traglia, et al. (2016), Gallant et al. (2018), and Mead and Magill (2017).

This study also represents a novel strategy for the dynamic implementation of evolving input information onto the background of long-term assessments. Marzocchi and Bebbington (2012) provide a detailed review of both long- and short-term probability forecasts of volcanic hazards. Long-term assessments are based on past eruption data and current tectonic information, while short-term assessments ideally include the monitoring of precursors.

A key aspect to both long- and short-term forecasting is that volcanic systems evolve through different states of activity. As such, hazard assessments should be updated and interpreted based on the current state of the volcano. First, efforts at this aim applied Bayesian Belief Networks as a powerful modeling tool (Aspinall et al., 2003). Several studies have explored long-term volcanic hazard assessments using Bayesian Event Tree methodology (Marzocchi et al., 2004, 2010; Sobradelo & Marti, 2010; Selva et al., 2010). Many recent modeling efforts have also explored possible implications of short-term eruption forecasting on hazard assessments (Sandri et al., 2012; Selva et al., 2014; Sobradelo & Marti, 2015). This paper presents an efficient, computationally judicious, and reliable statistical framework for evolving hazard assessments and their attendant uncertainties. Such an approach used in conjunction with those above has a strong potential to advance this field.

2. Background

Our approach and application to Long Valley hazard mapping provides an efficient strategy that uses statistical emulators to combine vent opening data and models and physical simulations of PDCs for probabilistic assessment of hazards. In this section we will briefly review each of the "ingredients."

2.1. LVVR

The LVVR is an area of bimodal basaltic-rhyolitic volcanism encompassing 4,000 km^2, east of the central Sierra Nevada mountain range (CA/NV, USA). It became active at ~4 Ma and at ~760 ka erupted about 650 km^3 of rhyolitic magma as the Bishop Tuff (Bailey, 2004; Hildreth, 2004). The deep structural subsidence inside the ring fault zone and shallower landsliding produced Long Valley caldera, a depression 32 km × 18 km (Bailey et al., 1976; Hildreth, 2017; Hildreth & Mahood, 1986). The Mammoth Mountain system developed since 230 ka on the southwest topographic rim of the caldera and includes a lava dome complex 3,400 m high, competing in height with nearby Sierran peaks (Mahood et al., 2010; Hildreth et al., 2014; Hildreth & Fierstein, 2016). The Mono-Inyo Craters volcanic chain and Mono Lake Islands are a nearly linear array of vents stretching north of the caldera for ~45 km (Bailey, 1989; Wood, 1983), with the most recent eruption ~ 1700 CE. A complete database of Late Quaternary eruptive ages in LVVR and their uncertainty is reported in Bevilacqua et al. (2018).

Tomographic and magnetotelluric studies (Achauer et al., 1986; Flinders et al., 2018; Foulger et al., 2003; Peacock et al., 2015, 2016) suggest that numerous, separate, midcrustal, potentially active magmatic sources (partial melt zones) lie in an irregular, N/S elongated zone, extending from Mono Lake to south of Mammoth Mountain. It is these multiple, restless, partial melt zones that are thought to supply the active Mono-Inyo and Mono Lake Islands volcanism.

The ongoing period of unrest in the LVVR started in 1978, with a magnitude 5.8 earthquake at the south edge of the caldera (Hill, 2006; Hill et al., 2017). A cumulative uplift of ~83 cm since 1980 has been measured, centered on the early postcaldera resurgent structure, aged ~570 ka (Hildreth et al., 2017). The uplift has been 3–5 cm since 2011 (Montgomery-Brown et al., 2015). Numerous episodes of unrest centered under

Mammoth Mountain have also been observed, including one in 2014 (Prejean, 2003; Shelly & Hill, 2011; Shelly et al., 2015). Diffuse CO_2 emissions at Mammoth Mountain claimed four lives in recent decades and killed ~40 km^2 of forest (Farrar et al., 1995; Gerlach et al., 1998, 1999). In contrast, relatively little degassing is currently measured in the Mono region (Bergfeld et al., 2015). Such a long and complex geophysical and geochemical unrest may culminate in a future volcanic eruption that could have a serious impact on the region (Kaye et al., 2009; Miller et al., 1982).

2.1.1. PDCs in the LVVR

The late Quaternary record of volcanism in LVVR indicates that both dome collapse (Merapi type) and column collapse (Soufriere type) PDCs have occurred. The Panum block and ash flow (BAF) occurred near the very end of the North Mono eruption sequence, after much of the dome building phase had ceased. It is typical in runout and volume for a BAF at LVVR and is the best exposed of these deposits (Dennen et al., 2014). Column collapse PDCs are documented for the South Mono, North Mono, and Inyo eruption sequences (Bursik et al., 2014; Miller, 1985; Sieh & Bursik, 1986) and, as is common, generally occurred near the end of the pyroclastic phases of these eruptions. Both BAF and column collapse PDC deposits occur in the late Quaternary Mammoth Mountain eruptive record, as well as in the Mono-Inyo record. BAF deposits crop out along California Highway 203 near Mammoth Mountain ski resort, and column collapse deposits occur in the record of the late (~70 ka) pyroclastic deposits documented by Hildreth et al. (2014). The volumes of potential PDCs are inferred from the data on past flows, as well as domes from which BAF could be generated (Appendix A). A typical volume is taken to be approximately 0.01 km^3, which represents the failure of a portion of an average LVVR dome. A maximum, "worst-case scenario" volume is very roughly estimated to be ~1 km^3. This volume represents the failure of an entire large Mono-Inyo dome or column collapse associated with the largest pyroclastic eruptions of the late Quaternary, the Mammoth pumice fall of unit rfp (Hildreth et al., 2014), or Wilson Creek formation layer B7 from Mono Craters (Yang et al., 2019).

2.1.2. Vent Opening Models for Long Valley

Because it is a tectonically complex region of diffuse volcanism, identifying likely locations of future vents is a key step in assessing volcanic hazards in the LVVR. It is instructive to quantify these likely vent locations and represent that analysis visually. To that end, one can construct a "map of vent openings" which is a distribution of vent openings (probability per unit of area) at each point within a region of interest. There are many examples of vent opening maps in the literature, all of which model the aleatoric variability (inherent randomness) of vent opening in a given region. Some of those maps are solely spatial assessments; that is, they model the vent locations conditioned on a new eruption occurring (Bartolini et al., 2013; Bebbington, 2013, 2015; Bevilacqua et al., 2015; Capra et al., 2011; Chapman et al., 2012; Connor et al., 2000, 2012; Magill et al., 2005; Marti & Felpeto, 2010; Mazzarini et al., 2013, 2016; Tadini et al., 2017). The most common approaches are based on the assumption that new vents will open up near past vent locations. Regions containing structural weakness (i.e., faults/fractures) can be incorporated probabilistically by treating geophysical or tectonic information as a model parameter(s) (Bevilacqua, Bursik, et al., 2017; Jaquet et al., 2012; Martin et al., 2004). Some vent opening maps are so-called *doubly stochastic*(Cox & Isham, 1980; Ogata & Akaike, 1982). That is, modeling the vent opening probabilistically reflects *aleatoric uncertainty* of new vent locations, but these probabilistic models themselves are subject to *epistemic uncertainties* which reflect model choices and/or limited data (Bevilacqua et al., 2015, 2016; Bevilacqua, Bursik, et al., 2017; Bevilacqua, Neri, et al., 2017; Selva et al., 2012; Tadini et al., 2017).

The hazard mapping tool we are proposing provides an efficient procedure for incorporating vent opening maps into probabilistic hazard maps, which represent the likelihood of threats from PDCs. The intuition of standard MC is useful—one can imagine sampling the vent opening map and then running TITAN2D at those sampled locations. The hazard mapping tool presented herein allows such analysis with a limited number of computationally intensive simulations. Further, it allows us to quantify how uncertainty in the vent opening maps impacts the resulting probabilistic hazard maps.

2.2. PDC Simulations Using TITAN2D

Depth-averaged physical models for granular flows introduced by Savage and Hutter (1989) and expanded on by Bursik et al. (2005), Iverson (1997), Iverson and Denlinger (2001), and Pitman et al. (2003) along with digital elevation models of a basal surface form a basis for modeling the depth and extent of dry pyroclastic flows. It should be noted that the following describes the dense basal flow. The associated surges (see, e.g., Ogburn et al., 2014) are not included in this model. A simplified description of this depth-averaged granular

flow model is as follows:

$$\frac{\partial}{\partial t}\begin{pmatrix} h \\ hv^x \\ hv^y \end{pmatrix} + \frac{\partial}{\partial x}\begin{pmatrix} hv^x \\ hv^{x^2} + \frac{1}{2}\kappa g^z h^2 \\ hv^x v^y \end{pmatrix} + \frac{\partial}{\partial y}\begin{pmatrix} hv^y \\ hv^x v^y \\ h^{v^{y^2}} + \frac{1}{2}\kappa g^z h^2 \end{pmatrix} = \begin{pmatrix} 0 \\ hg^x - \left(\frac{v^x}{\sqrt{v^{x^2}+v^{y^2}}}\right) h \tan\phi_{\text{bed}}[g^z + v^{x^2}\frac{\mathrm{d}b}{\mathrm{d}x}] - \text{sgn}(\frac{\partial}{\partial y}v^x)\frac{\partial}{\partial y}(\frac{\kappa}{2}\sin(\phi_{\text{int}})h^2 g^z) \\ hg^y - \left(\frac{v^y}{\sqrt{v^{x^2}+v^{y^2}}}\right) h \tan\phi_{\text{bed}}[g^z + v^{y^2}\frac{\mathrm{d}b}{\mathrm{d}y}] - \text{sgn}(\frac{\partial}{\partial x}v^y)\frac{\partial}{\partial x}(\frac{\kappa}{2}\sin(\phi_{\text{int}})h^2 g^z) \end{pmatrix} \quad (1)$$

where $h(x, y, t)$ is the depth of the flow at location (x, y) and time t. v^x, v^y, hv^x, and hv^y are flow velocities and depth-averaged momenta. (g^x, g^y, and g^z) are components of gravitational acceleration, and $\frac{\mathrm{d}b}{\mathrm{d}x}$ and $\frac{\mathrm{d}b}{\mathrm{d}y}$ represent terrain slopes of the basal surface $b(x, y)$. ϕ_{int} and ϕ_{bed} are internal and basal friction angles, and the terms including them reflect dissipation due to particle-particle interactions and flow over a basal surface, respectively. κ is a rheological parameter which combines the friction angles and a flow-dependent earth pressure coefficient.

Solutions to equation (1) are typically not available in closed form. TITAN2D software provides careful numerical approximations to the evolution of the flowing mass over a topography represented by a digital elevation model (Patra et al., 2005); those interested in using TITAN2D should see TITAN2D Mass-Flow Simulation Tool (2010). TITAN2D employs a second-order Godunov solver with an adaptive mesh. The digital elevation model provides boundary conditions for the flowing mass equations while initial conditions (initial volume, location, and velocity of the flowing mass) and parameters (internal and basal friction) must be provided by the user. Note that we model Mono Lake as a flat surface that PDCs would flow over. This modeling choice is consistent, to first order, with findings for PDC transport over water as documented in Carey et al. (1996), Edmonds and Herd (2005), Mandeville et al. (1996), and Sigurdsson and Carey (1989). More detailed modeling assumptions could be explored but are beyond the scope of the present work. Likewise, in this model each PDC is initiated with a cylindrical pile of material consistent with the volume of the flow under consideration. Although BAF and column collapse pyroclastic flows are often modeled in TITAN2D with different initial height to width ratios and basal friction angles, we have not varied these parameters accordingly in the present work, as our intent is not to produce an operational flow inundation hazard map but to explore and demonstrate a methodology for doing so. Such an approximation will likely not constrain the resulting PDCs as much as real topography near a source, and thus, one should take the resulting PDC footprints as conservative approximations for the dense underflow portion of the PDC. Note that we are not modeling inundation by any dilute, overriding surge cloud, which has considerably different dynamics and generally larger inundation footprint, from that of the underflow.

For the present study, *initial location* is of particular interest due to significant uncertainty in the vent opening location which we must explore for a probabilistic assessment of PDC hazards. Together these sets of inputs (initial conditions and parameters) represent a "scenario." An example of TITAN2D output from four scenarios is illustrated in Figure 1. Here the scenarios we consider include volumes of 0.01 and 1 km^3 with initial piles centered at (320242, 4167043) and (321071, 4166406) over UTM WGS84 zone 11. For each scenario from these four combinations, we plot the maximum flow depth at each location. The 1-km^3 cases, Figures 1c and 1d, demonstrate that modeling initiation with a cylindrical pile is relatively crude. That is, the flow is less constrained than it would likely be by detailed topography of the initiation. On the other hand, while modeling the morphology of potential future vents may be an insightful endeavor, it would also be a substantial study in its own right. To this end, it is worth noting that any physical modeling shortcomings will be inherited by the emulator. This does not diminish the power of the emulator—that many potential scenarios can be explored rapidly. This point can be seen in the 0.01-km^3 TITAN2D runs, Figures 1a and 1b, where a slightly different vent location results in one PDC that inundates locations close to Mammoth and another with a PDC that flows away from Mammoth. TITAN2D can be run on clusters of computers to speed up processing and handle large amount of simulated data. However, one TITAN2D simulation for a typical flow simulation can take around 30 min of compute time. This computational cost makes hazard threat assessment based on standard MC—probability calculations to carefully search scenario space for those that lead to inundation *for each map location* based on TITAN2D (or any computationally intensive physical model)—significantly expensive. Statistical emulators are a key tool to overcome this bottleneck.

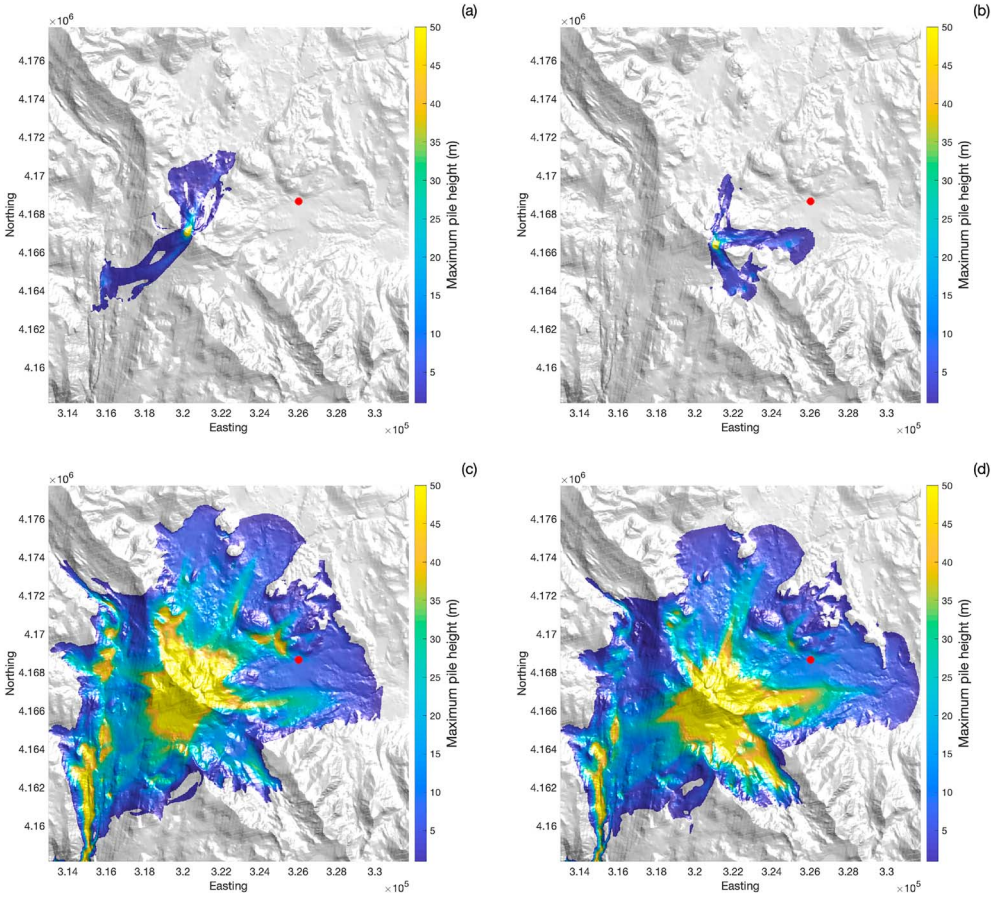

Figure 1. Estimated maximum flow depth of a pyroclastic flow in Long Valley for events of volume (a, b) 0.01 km^3 and (c, d) 1 km^3 (basal friction of 10.5° in each case) centered at (320242, 4167043; a, c) and (321071, 4166406; b, d). (Note that for visualization, yellow represents max height ≥50 m.) Both initial positions are near the top of Mammoth Mountain. A red dot is placed at the center of Town of Mammoth Lakes.

2.3. Statistical Emulators

Computer model emulators (also known as statistical surrogates) are effectively statistical models of computationally intensive simulators like TITAN2D (Rasmussen & Williams, 2006; Sacks et al., 1989; Santner et al., 2013; Welch et al., 1992). The benefit of using emulators is obvious—minutes or hours or days long simulations can be approximated by a function evaluation which is computationally free. A popular choice of an emulator is a separable Gaussian process (GP) fit to a relatively small set of simulator input-output pairs. For the problem at hand, we will consider an "input" to TITAN2D a set $\mathbf{x} = \{x_1, x_2, x_3, x_4\}$ where $x_1 =$ Volume, $x_2 =$ Easting coordinate of a vent location, $x_3 =$ Northing coordinate of a vent location, and $x_4 =$ basal friction. In this surrogate fitting approach, we will take our "data" to be the maximum height over the flow of a run of TITAN2D at every location of the map. We will then fit a GP to our scalar output—the max height data, h, at *each* location on the map (e.g., the discretized locations indexed $k = 1, \ldots, M$ max height output is reported). It is worth noting that, once the training runs of TITAN2D are complete, these M emulators can be fit in parallel (the approach we take here), or the so-called partial-parallel emulation can be applied (Gu & Berger, 2016). Considering one location, we will let $\mathbf{y}^S = [h_1, \ldots, h_N]^T$ be a vector of simulated output corresponding to each of N TITAN2D runs at scenarios in the design X_D. That is, $X_D = \{\mathbf{x}_j^D\}$, $j = 1, \ldots, N$. Then the GP surrogate is given by

$$Y(\mathbf{x}) = \mu(\mathbf{x}) + Z(\mathbf{x}) \tag{2}$$

where $Z(\cdot)$ is a constant variance, mean-zero spatial GP and $\mu(\cdot)$ is a user-specified mean function, typically taken to be linear or constant. In this work, we take the mean to be linear in the volume component and constant in the others. Like the mean, the choice of correlation structure is user specified. Typically, for

emulating computer experiments a separable (distinct correlation length scale for each input dimension) power exponential correlation or Matèrn correlation function is employed. Here we will use the Matèrn 5-2, given by

$$c(\mathbf{x}_i, \mathbf{x}_j) = \left(1 + \sqrt{5}d + \frac{5d^2}{3}\right) \exp\left(-\sqrt{5}d\right) \tag{3}$$

with $d = \sqrt{\sum_{m=1}^{4} (x_i^m - x_j^m)^2/\rho_m^2}$ and where ρ_m is the correlation parameter in the mth dimension of input space. We will define the $N \times N$ correlation matrix to be $\mathbf{R} = [R_{ij}]$ with elements $R_{ij} = c(\mathbf{x}_i^D, \mathbf{x}_j^D)$. Then we have the predictive mean and standard error given by

$$\tilde{h}(\mathbf{x}) = E[Y] = \mu(\mathbf{x}) + \mathbf{R}^T\mathbf{R}^{-1}\left(\mathbf{y}^S - \mu(\mathbf{x}^D)\right) \tag{4}$$

$$s^2(\mathbf{x}) = \sigma_z^2\left(1 - \mathbf{R}^T\mathbf{R}^{-1}\mathbf{R} + \frac{(1 - \mathbf{1}^T\mathbf{R}^{-1}\mathbf{R})^2}{\mathbf{1}^T\mathbf{R}^{-1}\mathbf{1}}\right) \tag{5}$$

where $\mathbf{1}$ is a length N column vector of ones and $\mathbf{R} = \left(c(\mathbf{x}, \mathbf{x}_1^D), \ldots, c(\mathbf{x}, \mathbf{x}_N^D)\right)^T$. Beyond these definitions, "fitting" a GP amounts to finding good estimates of parameters—σ_z^2, parameters in $\mu(\cdot)$, and parameters in the correlation structure, namely $\rho_1, \ldots, \rho_4$ for this work. The takeaway here is that we now have estimates of TITAN2D output from evaluating $\tilde{h}(\cdot)$ at scenarios where we did not run TITAN2D; for example, $\mathbf{x} \in D$, but $\mathbf{x} \notin X_D$. Further, $s^2(\cdot)$ quantifies how much uncertainty we introduce by replacing $h(\cdot)$ with $\tilde{h}(\cdot)$. In past work we have shown that the surrogates so constructed have small and quantifiable error in predicting $h(x, y)$ obtained by running TITAN2D. The surrogates are able to emulate TITAN2D, but situations where the simulator performance is poor (e.g., the rheology assumed is a poor match for the actual flow or where numerical grid choices are too coarse) are also reflected in the surrogate.

There are two natural approaches to implement emulator-based MC. Either one can directly sample Y (instead of h) in a MC calculation or one can utilize $\tilde{h}$ to search for *hazard contours* that divide the input space by separating scenarios that lead to hazard from those that do not. In this work, we will focus on the former approach but explore the latter to build visual intuition about the methodology.

3. Methodology: Building a Dynamic Probabilistic Hazard Map

Here we will illustrate the methodology for building a dynamic probabilistic hazard map that combines synthetic model-based data. The hazard mapping tool begins with a set of simulator runs, TITAN2D runs in our case. For the reader not familiar with using emulators of complex computer models, the set of training runs may not seem intuitive. Thus, we will describe motivation for and choice of the *design*, inputs/scenarios, to exercise our training runs. Then we will describe building the emulators, extracting inundation contours, and calculating inundation probabilities. We will walk through this process focusing on one map location, but it is important to keep in mind that once the initial training runs are complete, the rest of the process can (and should) be run in parallel. It is worth emphasizing that the probability calculations are done *post-processing* and thus can be run repeatedly to reflect both aleatoric and epistemic uncertainty in probability calculations. Further, if desired, these postprocessing probability calculations can be run for *any* level of PDC inundation, h_{crit}, that the user defines to represent a PDC inundation hazard.

3.1. Designs for Hazard Mapping

Recall that the inputs we vary for different runs of TITAN2D are the event volume, Easting and Northing of vent locations, and the basal friction coefficient. It is important to keep in mind that we are *not* assigning any probability to events in the design but that we need to account for regions of design space that we may want to sample later. To this end, in choosing the initial design of N distinct quadruplets $\{\mathbf{x}_j^D\}$, there are three concerns to weigh: covering input space for the whole map, accounting for tail events, and space filling.

Covering the input space for the whole map balances the fact that a "global" probabilistic hazard map is effectively the composite of many "local" problems. Intuitively, if a vent opens near a specific map location, even a relatively small volume PDC could be catastrophic to that location. In contrast if a vent opens, say, several kilometers away, it may take a very large volume of PDC to inundate the location of interest. Thus, each location on the map has a critical region of design space, and a global design relevant for the whole map must cover the union of these critical regions.

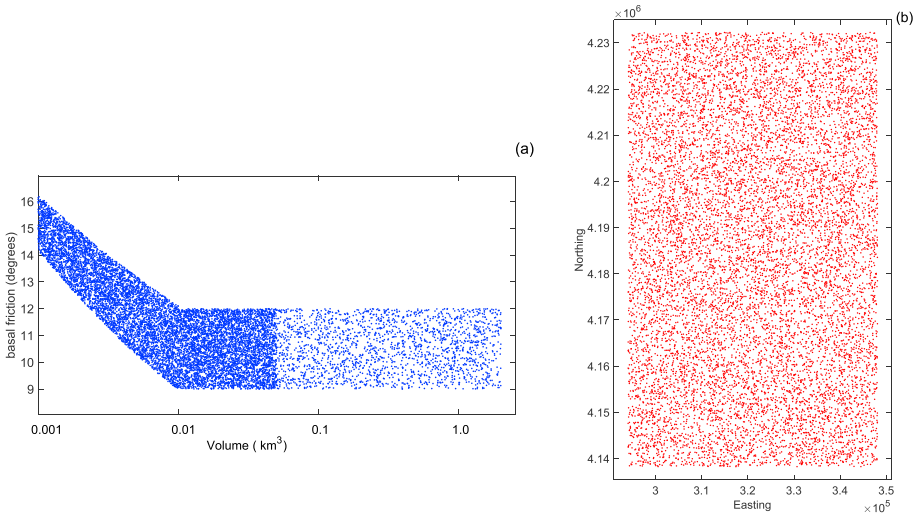

Figure 2. (a) Projections of the design points into the basal friction-volume plane and (b) the Northing-Easting plane.

Accounting for tail events reflects that we take a probabilistic approach to quantifying hazards in our design and include TITAN2D simulations that may correspond to very low probability events. Even if an event is low probability, if we have no samples (TITAN2D runs or approximations thereof) near that event in input/scenario space, corresponding probability calculations will be highly uncertain. To this end, we intentionally choose to sample a wide footprint of vent opening locations and volumes up to 2 km^3. In both cases these ranges go beyond what we think is realistic, even for a rare catastrophic hazard. To reiterate, no probabilities are assigned as this point in the process. That said, those points are included so that the support of any probability density function that we might use to describe aleatoric variability is appropriately sampled for the purpose of building emulators.

Space filling designs are the standard approach for training emulators of complex computer models (Santner et al., 2013). In this work, we use so-called maximin Latin Hypercube (LHC) sampling to choose our design points. These LHC designs spread out samples to ensure that the maximum distance from any point in design space to its nearest neighbor is (approximately) minimized and thus are called space filling designs (Johnson et al., 1990). Further, such LHC sampled designs when projected onto one axis of the input space (4-D, in our case) will appear to the eye as N distinct samples from a uniform distribution as opposed to using a grid which would result in $N^{1/4}$ evenly spaced grid points.

Projections of the $N = 12,000$ design points used to demonstrate the methodology are displayed in Figure 2. In the Northing-Easting plane, we extended the design beyond the support of both the simple Gaussian mixture model fit to previous vent locations and beyond the support of the sophisticated vent opening map model Bevilacqua, Bursik, et al. (2017). Nominally, basal friction is a material property which is approximated by the angle whose tangent is H/L (height drop of flowing mass/horizontal extent of runout; Hayashi & Self, 1992; Sheridan, 1979). In physical models, the basal friction effectively acts as a mobility parameter with lower values leading to more mobile flows (Charbonnier & Gertisser, 2009, 2012; Ogburn & Calder, 2017). The projection into the basal friction-volume plane is nonstandard in two ways. First, the density of design points is twice as high below 0.05 m^3 as it is above. This choice is motivated by the relative footprint of typical small versus large volume flows to ensure that every location on the map has some small volume PDCs that lead to inundation in that site's emulator design. Second, for volumes less than 0.01 km^3 the design is clearly not a rectangle and warrants further explanation. It is known that gravity-driven mass flow models such as TITAN2D do not accurately capture the mobility of large volume flows. Large volume flows are more mobile than material properties of the flowing material would suggest. The work of Ogburn (2014) and Ogburn and Calder (2017) shows that this model inadequacy can be mitigated by running TITAN2D with artificially low (in the material property sense) basal friction values and then achieving model flow mobility consistent with observed PDCs. The transition from basal friction values appropriate for small volume flows to those appropriate for large volume flows was modeled in Ogburn et al. (2016), and we based

the range of basal friction values on this relationship. For volumes larger than 0.01 km^3, we use a range from 9–12° which is again consistent with Ogburn (2014) and Ogburn and Calder (2017).

3.2. Emulating Hazard Contours and Calculating Hazard Probabilities

The process to construct emulators and to calculate hazard probabilities is identical for each location on the map, and thus, we will describe it for just one location of interest, a site within the Town of Mammoth Lakes (Mammoth). (Of course, to make a probabilistic hazard map, this process is repeated for each of M indexed points on the map.) Mammoth has been already the target of volcanic risk analysis of critical infrastructures (Kaye et al., 2009). Although the methodology does not require one to condition on a PDC occurring (Bayarri et al., 2009, 2015), for demonstration purposes and to focus on the impact of uncertain vent openings, we choose to do so. Thus, we seek to calculate the probability of inundation conditioned on an event of volume v having occurred and visualize the impact of vent opening models on probabilistic hazard maps. We can calculate this probability for any volume, but we will focus on two volumes, $v = 0.01$ km^3 and $v = 1$ km^3 which we take to represent a typical PDC for LVVR or a worst-case scenario PDC, respectively. A detailed analysis of potential PDC volumes, based on previous eruptions, is reported in Appendix A. Note that we are not endorsing gravity-driven, shallow water like flow models such as TITAN2D as "good" models for flow events resulting from column collapse, but our approach is agnostic to physical/computational models. That is, further analysis could be done with a different model specifically describing large mass flows from column collapse events, including multiphase and 3-D effects (e.g., Iverson & George, 2014; Neri et al., 2003; Pitman & Le, 2005; Valentine & Wohletz, 1989; Valentine & Sweeney, 2018).

We treat the vent location probabilistically, and we can consider any probability density function, $p(E, N)$, where E and N are the Easting and Northing coordinates of vent opening. Such an exploration is twofold. We can consider different aleatoric models of the vent location and the resulting probabilistic hazard maps under each. Likewise, by the same approach, we can consider epistemic uncertainty in a single probabilistic model of vent opening.

Calculating a hazard probability amounts to doing an integral. For the Town of Mammoth Lakes (henceforth referred to as Mammoth and indexed by the subscript k), we have

$$P_k(\text{inundation}|\text{event volume} \quad V = v \quad \text{occurs}) = \int_{\mathcal{M}} \mathbf{1}_{h_k \geq 1m} \quad p(E, N)\mathrm{d}E\mathrm{d}N \tag{6}$$

where $\mathcal{M}$ is defined by $E \in [294000, 348000]$, $N \in [4138000, 4232000]$ and $\mathbf{1}_{h_k} \geq 1$m is an indicator function that is 1 if the flow height meets or exceeds 1 m at Mammoth and 0 otherwise. (Note that 1 m is a user-defined choice to represent PDC "inundation," likewise 0.25 or 0.5 m would be reasonable choices.) In a standard MC approximation, it can be written as

$$P_k(\text{inundation}|\text{event volume} \quad V = v \quad \text{occurs}) \approx \frac{1}{N_{\text{samp}}} \sum_{i=1}^{N_{\text{samp}}} \mathbf{1}_{h_k(E_i, N_i) \geq 1m} \tag{7}$$

where $E_i, N_i \sim p(E, N)$. Note that $h_k(E_i, N_i)$ represents the maximum height of the flowing mass resulting at Mammoth for a PDC of volume v from a vent located at (E_i, N_i). This MC approximation would be prohibitively expensive if each MC sample required a TITAN2D run. In other words, the computational expense of this calculation is in evaluating the indicator function. To overcome this limitation, we utilize an emulator of the max flow height of TITAN2D which we can use to approximate evaluations to this indicator function rapidly. That is, we replace $h_k(E_i, N_i) \geq 1$ m in the indicator function in equation (7) with $\tilde{h}_k(E_i, N_i) \geq 1$ m. Note also that we can quantify the uncertainty of using the emulator in place of TITAN2D by sampling the GP given by equation (2) for Mammoth directly instead of utilizing the GP predictive mean. In this case, we replace the right-hand side of equation (7) as

$$\frac{1}{N_{\text{samp}}} \sum_{i=1}^{N_{\text{samp}}} \mathbf{1}_{h_k(E_i, N_i) \geq 1m} = \frac{1}{N_{\text{samp}} N'_{\text{samp}}} \sum_{i=1}^{N_{\text{samp}}} \sum_{j=1}^{N'_{\text{samp}}} \mathbf{1}_{H_k^j(E_i, N_i) \geq 1m}$$

where H_k^j is the jth draw from the GP fit at Mammoth and the additional MC step to quantify the uncertainty induced by replacing TITAN2D with a GP has $N\text{samp}'$ samples.

To construct this emulator, we first begin by identifying a *subdesign* or a subset of the full design that is critical for Mammoth. For any location of interest, most of the TITAN2D runs from the full design will

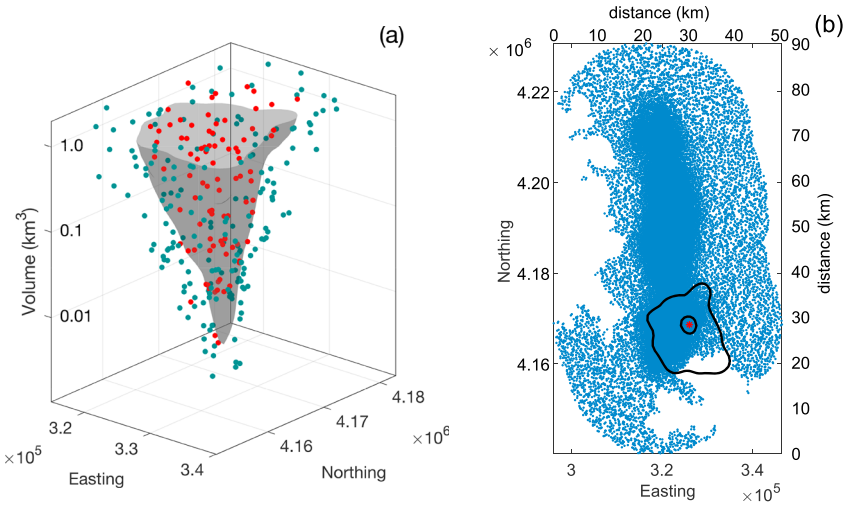

Figure 3. (a) Gray surface represents the level surface corresponding to $\mathbf{x} \in D$, where $\tilde{h}(\mathbf{x}) = h_{\text{crit}}$, x-y plane is Easting and Northing, and the z axis is volume on a log scale. Green (zero height) and red (positive height) dots denote training runs of TITAN2D used to construct the emulator at Mammoth; for example, $\mathbf{x} \in X_D^k$. Runs initiated at a given $\mathbf{x}$ and median basal friction value, which fall within the contour defined by constant volume planes parallel to the x-y plane, lead to inundation. (b) Level curve evaluated at $v = 0.01$ km^3 (inner black curve) and $v = 1$ km^3 (outer black curve), effectively visualize slices of the surface on the left. Blue dots are 10^5 random samples of the vent location according to the model in Bevilacqua, Bursik, et al. (2017). For a pyroclastic density current of given volume initialized at a design point, vents within the respective black curve will result in inundation at Mammoth (red star).

result in *no flow* at that location. Thus, we will discard most of the zero-flow runs and keep only those that are closest (in design space normalized to a unit hypercube) to TITAN2D runs that result in a positive maximum flow height. Typically, the number of "critical" design points relevant to a location of interest is approximately 2 orders of magnitude smaller that the full design and for Mammoth example is 270. (Note that this approach to choose a subdesign is independent of the user-defined inundation threshold, h_{crit}.) Again, denoting Mammoth with the index k, the resulting subdesign $X_D^k \subseteq X_D$ in hand, we then move onto building emulators and constructing hazard contours for Mammoth.

To help visualize this process, it is useful to think of the emulator's role in the probability computation in another fashion. An emulator helps us identify a curve (or surface) that separates events in scenario space that lead to inundation from those that do not. Toward this end, we build an emulator of the maximum flow height at Mammoth utilizing only $\mathbf{x}_j \in X_D^k$ and output from the corresponding TITAN2D runs $\mathbf{y}_k^s = \{h_k^s(\mathbf{x}_j)\}$. We find the predictive mean of the resulting emulator by using this data in equation (4). We then use the surrogate mean function, $\tilde{h}_k(\mathbf{x})$, to determine a level surface in design space, that is, $\mathbf{x} \in D$ such that $\tilde{h}_k(\mathbf{x}) = h_{\text{crit}}$. Figure 3a shows this level surface for Mammoth in volume×Easting×Northing space along with the critical design points used to fit the emulator at Mammoth (Note that the level surface is evaluated at the median basal friction value). Figure 3b shows contours in Easting×Northing space that result from evaluating this level surface at specific volumes—here we focus on $v = 0.01$ km^3 and $v = 1$ km^3. About 10^5 random samples for the PDC initiation vent locations are also plotted on Figure 3b. Those are sampled according to the probabilistic model detailed in Bevilacqua, Bursik, et al. (2017) and reviewed in section 4.2 of this study. We remark that the sharp boundary of the vent opening region depends on the uniform map layer included in the model. The boundary is located at a 20-km range from past vent locations, excluding regions above 3,000 m if not within a 5-km range from past vents. This choice is discussed in the vent opening study, and it is relevant to mitigate the possibility of PDC unrealistically initiating over nonvolcanic plateaus or peaks in the Sierra Nevada range. (Note that we use physical information where available to restrict the analysis to only plausible inputs.) We also remark that ~ 90% of the initiation points displayed in the figure are localized along the Mono-Inyo volcanic chain, close to Mammoth Mountain, or over Mono Lake islands.

Using such a level curve in place of an indicator function in the MC calculation in equation (12) amounts to sampling a probability density function for vent locations, $p(E, N)$, and counting the fraction of vents that fall within the level curve. As such probability calculations are now a postprocessing step that have computational demands only restricted by the sampling.

3.3. Computational Advantages of Emulator-Based MC

The most obvious advantage of using emulator-based MC is that TITAN2D runs each take O(minutes)-O(hours) on super computers (depending on the domain, the local topography, the numerical error tolerance, etc.) while emulators take a fraction of a second to evaluate on a laptop. This speedup is perhaps not obvious in light of the extensive set of training runs we presented. LVVR covers 4,500 km^2 and getting adequate coverage of possible vent locations to build emulators required $N = 12,000$ training runs. For any location of interest in LVVR, there are roughly N/10 runs whose vents are near enough to the location of interest to get any flow to that location for the largest volume we considered (a 2-km^3 flow). Of course, run at smaller volumes, many of these runs still result in no flow at the location of interest. For fitting an emulator, as we described for Mammoth, we need roughly an order of magnitude fewer runs (270 in that case.) Of course, nearby locations will share "important" runs, but the large design required at LVVR is due to the large spatial domain of that area *and* inputs to the emulator that vary spatially (e.g., vent locations.)

The power of replacing standard MC with emulator-based MC can be seen from investigating error analysis of MC calculations. Our exceedance probability calculations are just integrals and in the most generic sense can be written as

$$E_f[G] = \int_{-\infty}^{\infty} g(x) f(x) \mathrm{d}x \tag{8}$$

where, in analogy to equation (12), $g(\cdot)$ is the indicator function and $f(\cdot)$ is a probability density function describing our aleatoric uncertainty about potential scenarios. If we define the error in our MC simulation as

$$e = \left| \frac{1}{N} \sum_{i=1}^{N} g(X_n) - E_f[G] \right| \qquad X_i \sim f \tag{9}$$

then by Chebyshev's inequality, we have an error estimate given by Papoulis and Pillai (2002) and Ross (2012)

$$e \propto \frac{\sqrt{\mathrm{var}_f[G]}}{\sqrt{N}}. \tag{10}$$

Equation (10) tells us that there are two mechanisms to reduce the error in an MC estimator. The first is to increase the number of MC samples. Note that since MC is $O(N^{-1/2})$, we require a hundred fold increase in to get 1 order of magnitude improvement in the error of the estimator. This is clearly problematic if each additional sample requires an O(min)-O(hr) computation. The other mechanism to reduce the error is to reduce the variance of the MC estimator, $\mathrm{var}_f[G]$. Importance sampling is a powerful variance reduction technique, and there is a well-known result that the optimal importance sampling distribution is $\tilde{f}(\cdot) \propto f(\cdot)g(\cdot)$ (Bucklew, 2010). For our dynamic probabilistic hazard mapping approach this has two implications: through $f(\cdot)$, variance reduction depends on the choice of aleatory model and through $g(\cdot)$ variance reduction is location dependent as the indicator function is location dependent. Thus, there is no obvious systematic way to improve MC estimates for calculating inundation probabilities for a whole map at once via smart sampling schemes using a fixed and small number of samples. And if somehow we found one, it would be suboptimal if we wanted to consider the impact of utilizing other probability distributions of scenarios as we do to quantify epistemic and aleatoric uncertainties. Alternatively, one could explore location-dependent importance sampling schemes by using the estimate of the indicator function provided by the emulator in $\tilde{f}(\cdot) \propto f(\cdot)g(\cdot)$.

4. Results and Discussion: Dynamic Probabilistic Hazard Maps in the LVVR

The hazard mapping tool proposed here provides a systematic and efficient strategy to combine physical modeling and statistical modeling for forecasting resulting volcanic hazards. This approach provides *both* state of the art hazard forecasting through probabilistic hazard maps *and* a mechanism to quantify attendant uncertainties.

4.1. Quantifying Aleatoric Uncertainty

The process of constructing emulator-based probabilistic hazard maps as described in section 3 is independent of any specific vent opening model. Ultimately, a probability model for vent opening that reflects the

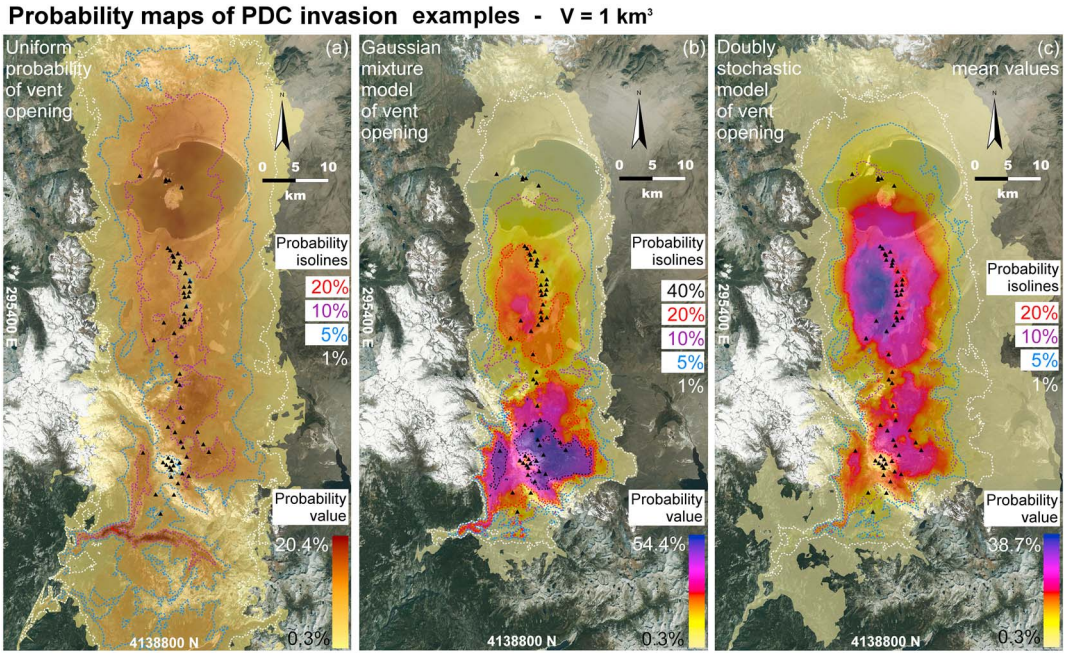

Figure 4. Dynamic probabilistic hazard maps conditioned on a PDC event of volume of 1 km^3—a "worst-case scenario" PDC at Long Valley volcanic region—and based on (a) a uniform vent opening probability distribution, (b) a Gaussian mixture model based on known past vent locations, and (c) the mean values of the doubly stochastic model in Bevilacqua, Bursik, et al. (2017). Black triangles mark past vent locations in the last 180 ka (Bevilacqua, Bursik, et al., 2017). PDC = pyroclastic density current.

aleatoric variability of the system must be chosen and the resulting map quantifies that choice of aleatoric variability via the hazard probability calculation in equation (12).

The dynamic probabilistic hazard mapping tool lets one investigate the impact of aleatoric modeling choices on hazard forecasts. Here we walk through how a typical probabilistic modeling process might proceed. Thus, we start with an uninformed, naive model of vent opening to reflect aleatoric variability, namely, a uniform probability of vent opening over a given region. Then we proceed to consider a simple vent opening model based on previous vent locations in LVVR. Finally, we consider a sophisticated model that incorporates both previous vent opening data and other geological data that indicate areas of possible new eruptions. The key here is that one does not have to wait for "the best aleatoric model" to be developed to devise hazard forecasts, and thus, one can see the impact of modeling choices on those forecasts.

Figure 4 shows three examples of probabilistic hazard maps (PHM) according to these very different vent opening probability models and assumes an event of volume of 1 km^3, for example, a worst-case scenario PDC in LVVR (see Appendix A). (Note that in this example and throughout this section, we take h_{crit} =1 m and evaluate the emulator at the median basal fiction value, 10.5°.)

In detail, Figure 4a adopts a uniform vent opening probability distribution of a rectangular domain encasing the past vent locations over the region [313000, 33100]× 4140000, 4231000]. The hazard levels are significantly spread and influenced by topography, with 20% reached in the canyon of the Middle Fork of the San Joaquin River. Figure 4b adopts a Gaussian mixture model with four components fit to past vent locations. Hazard values are more peaked, with values >50% in the area of Mammoth Mountain and >20% West and South of the Mono domes, as well as in the West Moat of Long Valley caldera. Figure 4c adopts the mean values of the doubly stochastic model under consideration.These data—samples from the doubly stochastic model–are publicly available here (Bevilacqua et al., 2019). Hazard values >35% are estimated for the area West of Mono Domes and values >20% in the Inyo Domes region, the West Moat of Long Valley caldera, and all around the Mono chain including the South portion of Mono Lake. In summary, the vent opening model has a profound effect on the PHM values—on the maximum hazard levels reached, on where they are located, and on the spatial extension of the area exposed. We imagine that this kind of analysis could

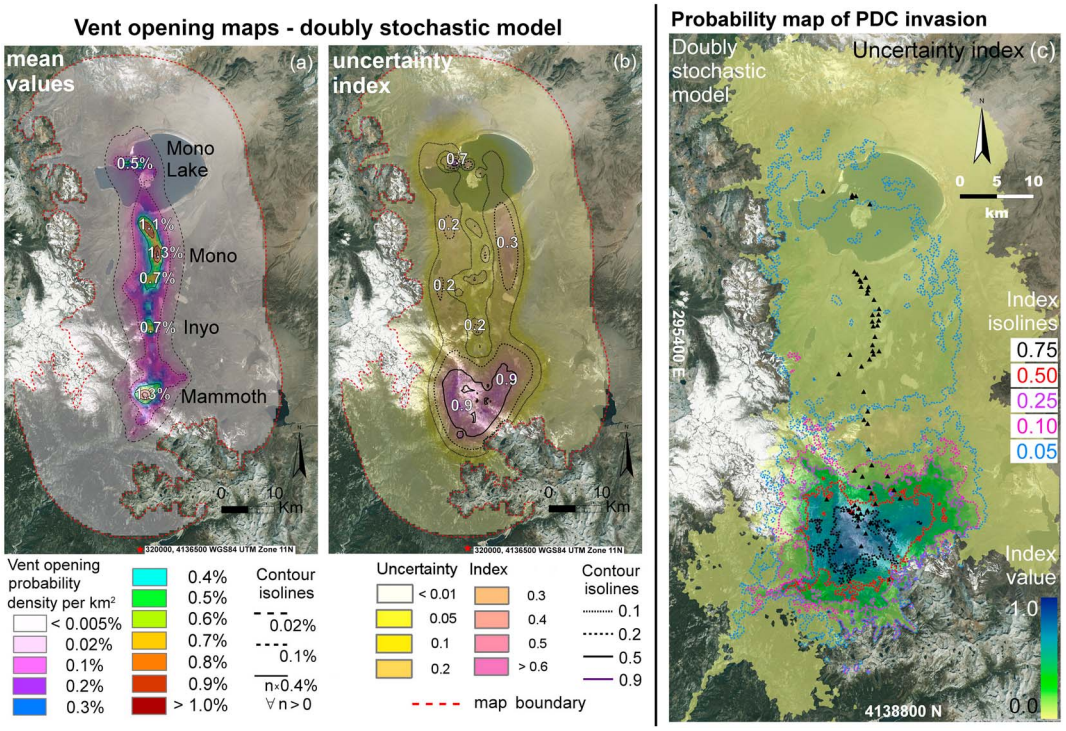

Figure 5. (a, b) Vent opening probability maps for Long Valley volcanic region based on Bevilacqua, Bursik, et al. (2017). In (a) we show the mean values of the probability per square kilometer and in (b) the uncertainty index associated with those values. In (c) we show the uncertainty index of the related probabilistic hazard map (Figure 4c). Black triangles mark past vent locations in the last 180 ka. PDC = pyroclastic density current.

be very useful not as a finished product but as an aid for understanding and communicating the impacts of aleatoric uncertainties through the modeling process.

The power of this methodology lies in the ability to rapidly construct maps such as those in Figure 4. Once TITAN2D training runs are done and emulators are constructed, producing new probabilistic inundation maps takes roughly 5–10 min on a cluster. Thus, it is very easy to explore different aleatory probabilistic descriptions of scenarios. In particular, we believe that this could be a useful tool to incorporate monitoring data into such probabilistic inundation studies. Aleatory models can be updated/adjusted to reflect new information from monitoring data and then fed through the probabilistic hazard mapping process to visualize the impacts of these updates on probabilistic inundation maps. This approach is faster than running a few one-off TITAN2D flows representing scenarios consistent with monitoring data. Further, and more importantly, this approach is statistically robust as incorporates probabilistic descriptions of potential scenarios.

4.2. Probabilistic Hazard Analysis in LVVR and Quantifying Epistemic Uncertainty

In the following description, we focus our hazard analysis by utilizing the vent opening map(s) described in Bevilacqua, Bursik, et al. (2017). This is the most reliable vent opening model available to us, in terms of volcanological knowledge. In this model, the authors consider "map layers" associated with three different conceptual models and combine them with weights found using a Bayesian Model Averaging approach.

The first model focuses exclusively on the distribution of past vents and describes the expected distance to new eruptive vents relative to past vent locations. The second model assumes that fault outcrops (i.e., mapped faults) are related to future vent locations. Only structures which are likely to have previously interacted with the rise of magma are considered, highlighting the preferred routes of previous dike intrusion. The third model is a uniformly distributed probability map inside a conservative (i.e., large) distance range. It considers the effect of potentially missing information such as the presence of unknown past vents or any vent opening dynamics missed by the other models. Note that the model averaging weights themselves are uncertain, reflecting the main effects of epistemic uncertainty in the doubly stochastic framework. In particular, the sources of epistemic uncertainty include the unknown relationship between events in

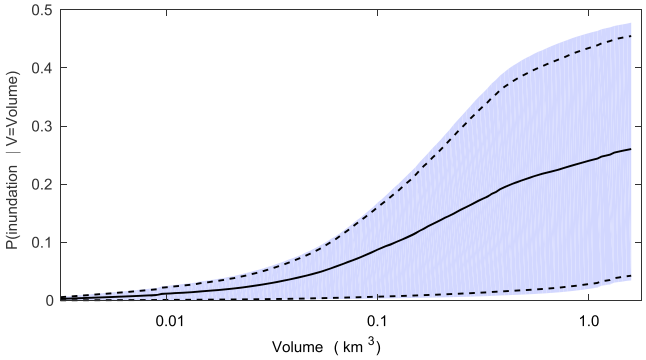

Figure 6. Probability of inundation hazard at Mammoth as a function of pyroclastic density current volume. The mean hazard probability is plotted as a solid black curve. The full spread of probabilities reflecting epistemic uncertainty in the vent opening model is shading in light purple, while the 95% credible interval is within the black dashed curves.

the Northern (Mono) part of the region relative to those in the Southern (Mammoth) part, the unknown expected distance to future vents from past locations or from fault outcrops, and the chance of unmapped faults.

Figure 5 displays this state-of-the-art vent opening map along with probabilistic hazard maps that utilize the vent opening model under consideration. We have 250 sample vent opening maps from this model, each of which has different weights to combine the map layers in the Bayesian Model Averaging approach. These map samples reflect epistemic uncertainty in the vent opening model and that epistemic uncertainty varies spatially. Figure 5a displays the mean values of the vent opening pdf per square kilometers. Maximum values of 1.3% probability per square kilometers are located along the Mono chain and around Mammoth Mountain. Secondary maxima above 0.5% per square kilometers are on the Inyo chain and on the islands and North shore of Mono Lake. Positive values, but <0.02% per square kilometers“ are spread on a wide region. Figure 5b shows a description of variability due to epistemic uncertainty among the vent opening map samples given by the uncertainty index

$$U(x,y) := \begin{cases} \lambda \cdot \frac{q_{95}(x,y) - q_5(x,y)}{q_5(x,y))}, & \text{if} \quad q_5(x,y) > 0 \\ 0, & \text{otherwise} \end{cases} \tag{11}$$

where (x, y) are the geographic coordinates, q_n is the nth percentile of the vent opening pdf, and λ is a normalization constant such that $\max(U) = 1$. The uncertainty index is a new definition and maps the uncertainty as a relative error. We note that the uncertainty index is zero when the 5th percentile is (exactly) zero. However, in our case, if that is happening then the 95th percentile is also zero, thus the uncertainty is zero. The index shows that the maximum uncertainty is localized in the Mammoth Mountain area, but significant uncertainty affects the vent opening probability in Mono Lake and to the East of the Mono region.

Figure 5c displays the uncertainty index of the PHM of Figure 4c. Uncertainty is significantly peaked around Mammoth Mountain, the West Moat of Long Valley caldera, and in the canyon of the Middle Fork of the San Joaquin River. Before moving on to further hazard analysis, we describe in more detail how the emulator-based hazard mapping tool is used to construct Figures 4c and 5c.

The probabilistic hazard mapping approach presented here can readily capture the effects of epistemic uncertainty on a forecasted PDC hazard map. To do so, we construct a probabilistic hazard map using equation (7) for each of the 250 sample vent opening maps. That is, we repeat the MC calculation for each of 250 $p(E, N)$, but the added computational expense is negligible when using the emulator in place of TITAN2D. And for each location of interest (e.g., Mammoth), the emulator only needs to be constructed once. Considering Figure 3b, the analogy here is that each sample of the vent opening map will yield a different set of vent samples that can be evaluated with the same emulator. That is, the blue dots will change from one map sample to the next but not the black contours.

We can construct dynamic probabilistic hazard maps conditioned on any PDC volume. This allows us to explore the probability of PDC hazard inundation as a function of volume under any vent opening map. Figure 6 shows this probability of catastrophic hazard (here defined as a flow exceeding $h_{\text{crit}} = 1$ m) as a function of PDC volume at Mammoth. The epistemic uncertainty inherited from the vent opening model is also explored as a function of volume and included in this figure. It is worth noting that the mean hazard probability has the steepest slope between volumes of 0.1 and 0.3 km^3. This kind of analysis is useful in thinking about the sensitivity of hazard forecasts to an uncertain input scenario even when a probabilistic model of that scenario is not readily available.

In Appendix A we explore four models for volume (two data sets and two models for each.) We will not present full probabilistic hazard maps using those models as the models are still preliminary. That said, incorporating volume models into the probability of inundation calculation is quite straight forward. Thus, emulator-based MC approach allows us to explore the impacts of epistemic uncertainty in the vent opening

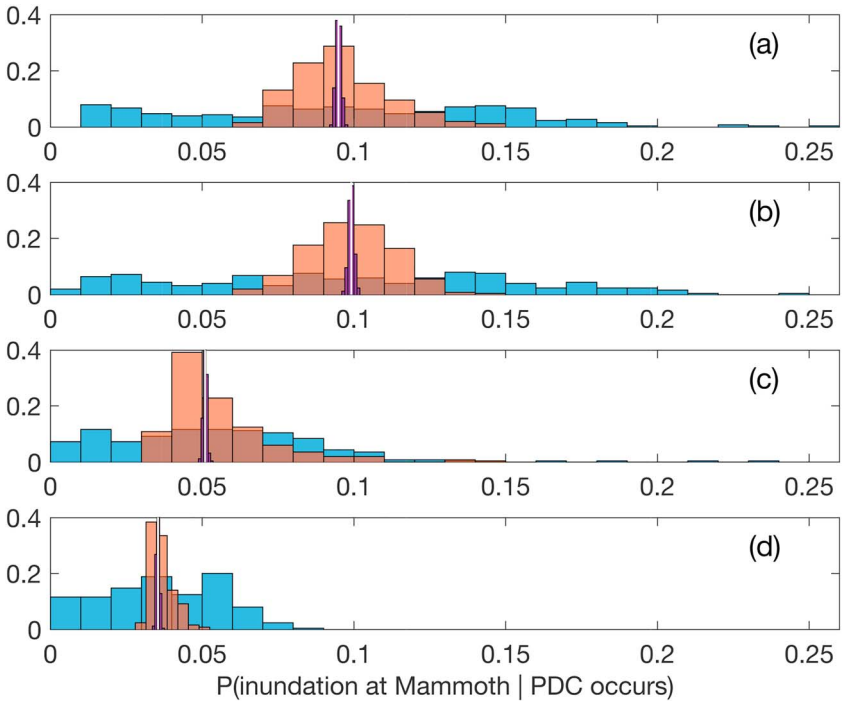

Figure 7. Histograms of probabilities of inundation at Mammoth reflecting epistemic uncertainties are depicted above. In each figure, the blue histograms reflect uncertainty in the vent opening model and volume model (Case 1), the salmon histograms reflect uncertainty only in the volume model (Case 2), the purple histograms fix both models, and the white bars represent the mean inundation probability in each case. Each figure above represents one model/volume data set choice: (a) Pareto distribution, past dome data set; (b) Lognormal distribution, past dome data set; (c) Pareto distribution, PDC data set; and (d) Lognormal distribution, PDC data set. PDC = pyroclastic density current.

models (as above) *and volume models* on the probability of inundation. To isolate the impacts of epistemic uncertainty on the hazard forecast at Mammoth, let us consider an updated version of equation (7), namely,

$$P_k(\text{inundation} \mid \text{PDC occurs}) = \int_{\mathcal{M}} \mathbf{1}_{h_k \geq 1m} \quad p(E,N)p(V)\mathrm{d}E\mathrm{d}N\mathrm{d}V \tag{12}$$

Here $p(V)$ has uncertain parameters, and we can either plug in the average parameters or sample those parameter values to get a family of $p(V)$s much as we have a family of 250 vent opening maps as described above. For each $p(E,N)$ and $p(V)$ under consideration, we will take $N_{\text{samp}} = 10^5$ MC samples of $\{E,N,V\}$ as to diminish the effects of MC error on the calculations of P_k (recall that k was the index that denotes Mammoth.) We explore three cases and present histograms of each: (1) sample parameters in $p(V)$, sample vent opening maps $p(E,N)$; (2) sample parameters in $p(V)$, fix $p(E,N)$ (as full posterior); and (3) fix $p(V)$ at median parameter values, fix $p(E,N)$. In each of the three cases, and for each of the four volume models under consideration, we repeat the MC calculation 250 times and collect histograms of hazard probabilities that illustrate the impacts of the various sources of epistemic uncertainty. These results are summarized in Figures 6 and 7. The epistemic uncertainties for models fit to past dome deposit data (a and b) are relatively similar to each other. As anticipated from the heavy-tailed nature of the Pareto distribution (a) the right "tail" of the histograms extends further than they do in the lognormal case (b; for both histograms 1 and 2), although the lognormal has a higher mean inundation probability. In contrast, the epistemic uncertainties for models fit to only PDC deposit data (c and d) behave quite differently from each other. In the Pareto case (c) there is a dramatic impact on the right tail of both probability histograms (1 and 2). The mean inundation probability estimate for the Pareto case is about twice that for the lognormal case. Further, the mean value in the Pareto case barely falls in the support of histogram (2) for the lognormal case (Figure 7).

Note that Figures 6 and 7 represents 300 million individual MC samples which would be computationally infeasible if a new TITAN2D run were required for each but takes roughly 2 hr (10 min for each of 12 histograms) to complete on a laptop. As with the dynamic probabilistic hazard maps presented in this paper, such an analysis could be run for each site in parallel with distributed jobs on a cluster.

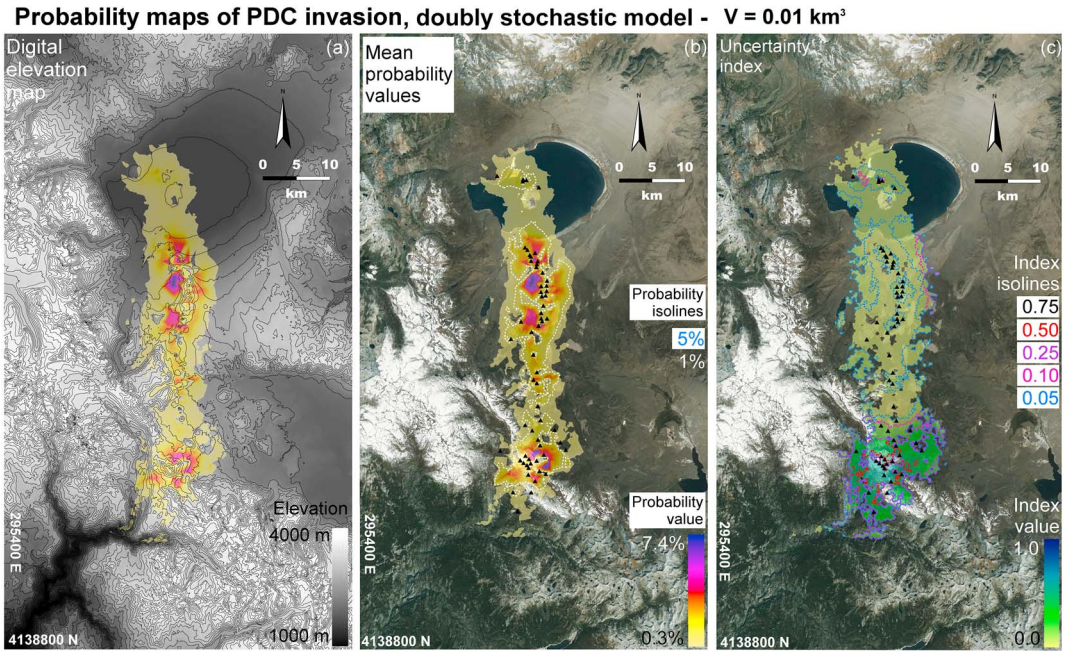

Figure 8. (a, b) Mean probabilistic hazard based on the model of Bevilacqua, Bursik, et al. (2017) and conditioned on a PDC event of volume of 0.01 km^3 plotted over a topographic map in (a), over a satellite image in (b; note that we are presenting both as snow cover obscures some of the topography that drives inundation toward the southwest of Mammoth Mountain), (c) the corresponding uncertainty index of the probabilistic hazard map. Black triangles mark past vent locations in the last 180 ka. PDC = pyroclastic density current.

We remark that, even if we focus on volumes larger than $V = 0.001$ km^3 (see Figure 2a), the chance of future, smaller PDCs may not be negligible, because they are difficult to distinguish in the ash layers and often ancillary to larger flows (see Appendix A). However, the footprints of such flows are quite geographically constrained and we suspect a resulting PDC hazard forecast map would differ little from the vent opening model under consideration. Instead, for larger PDCs, the interplay of vent opening, topography, and flow physics is usually nontrivial. From Figure 6 it is apparent that rare yet large-scale events are those most likely to lead to catastrophic hazards.

Assuming $V = 0.01$ km^3, Figures 8a and 8b show the mean of our 250 probabilistic hazard maps over two representations of topography, while Figure 8b shows the uncertainty index, which describes variability among the 250 probabilistic hazard maps. Note that the palest yellow which dominates the left/middle figures represents a probability of hazard of less than 1%. Some of this area reflects the uniform component of the vent opening model (and hence location of possible future PDCs) which itself represents epistemic uncertainty. Taking such uncertainties into account renders these resulting probabilistic hazard maps as rather conservative. The mean hazard values are ≥1% only in a range of ~5 km from the past vents of Mammoth Mountain, Mono-Inyo domes, and Negit Island in Mono Lake. Hazard values >5%, with maximum at 7.4%, are located in the northwest of the Mono chain and at the eastern base of Mammoth Mountain, where Mammoth is situated. The uncertainty index is again peaked around Mammoth Mountain and surrounding areas, with secondary maxima to the east of Mono domes and in the northwest of Mono Lake.

5. Conclusion

We have constructed probabilistic hazard maps for PDCs of volumes 0.01 and 1 km^3. These volumes volumes are representative of the largest PDC volumes seen in the LVVR in the Holocene and the late Quaternary, respectively (Sieh & Bursik, 1986). The probabilistic hazard maps represent the likelihood, with uncertainty, that a flow of the given volume would inundate a locality, assuming the physical model is appropriate and given an eruption can happen at vent locations consistent with the aleatoric model of vent locations from Bevilacqua, Bursik, et al. (2017) and eruptive behavior typical of the late Quaternary period. For PDCs of volumes of the range ~0.01–1 km^3, the inundation could likely pose a risk to large engineered structures and complexes such as dams, bridges, and entire ski resorts in addition to roads and minor, nonengineered

structures, such as houses. We further illustrated how, using this emulator-based strategy, we can incorporate probabilistic models of volume and vent opening into such hazard calculations. Further, this methodology enables visualization of the impact of scenario model epistemic uncertainties on the probability of inundation as we illustrated at Mammoth. The impact of other uncertain inputs can be analyzed in a similar fashion. If combined with a temporal vent opening map (Bevilacqua et al., 2018), the data in these maps could be used to generate a map of probability of inundation on an annualized, centennial, or millennial basis, whichever is more appropriate to a given engineering or civil defense application.

In the present contribution, we have discussed the role of statistical surrogates (emulators) in volcanic hazards assessment and probabilistic hazard map construction for the LVVR, CA.

The important points of the exercise are the following:

- Emulators provide a flexible tool for the construction of probabilistic hazard maps from a particular type of volcanic phenomenon (in the present case, PDCs), given aleatory and epistemic uncertainty in the position, persistence, and characteristics of the potential source locations. New, computationally costly numerical model (simulator) runs are not needed as knowledge of the source improves with continued development of geologic information on past events or geophysical information about evolving unrest. Moreover, the direct characterization of the critical output as a function of possible eruption scenarios (in terms of location, volume, and mobility of flows) compensates for the lack of knowledge of many aspects of the physics.
- Dynamic hazard maps allow one to efficiently examine the impact of various sources of uncertainties on probabilistic hazard forecasts.
- Given the ability to develop a hazard map quickly, we have shown that there is a role for near real time, probabilistic hazard forecasting and hazard mapping as a situation of unrest, or continued generation of pyroclastic flows evolves.
- The TITAN2D modeling tool here makes many simplifications and does not capture the effect of several significant phenomena (e.g., entrainment and flow stopping criteria) for which data are unavailable and/or the physics is poorly understood. Nevertheless, the careful accounting of uncertainty in the dynamic probabilistic hazard map construction outlined here is insightful and implicitly overcomes some of the inadequacy of the model while providing support for decision making by experts.
- Potential further investigations include the following:
  - As part of a holistic probabilistic hazard study at LVVR, calculating frequency and volume models of flow hazards and incorporate those using the presented methodology to make probabilistic hazard maps and study the impacts of various uncertainties (see Appendix A for a preliminary analysis of past volumes.)
  - Making it possible for civil authorities to communicate probabilistic hazard forecasts and uncertainties as part of a hazard analysis or risk assessment.
  - Taking temporal eruption frequency into consideration, providing time-space assessments (Bebbington & Cronin, 2011; Bebbington, 2013; Bevilacqua et al., 2016; Connor & Hill, 1995; Jaquet et al., 2017) and even volume-space assessments (Bebbington, 2015; Bevilacqua, Neri, et al., 2017).

We reiterate that, although details in this work are specific to PDCs and the LVVR, the approach we present here is quite general and flexible. That is, a similar emulator-based dynamic hazard mapping strategy could be applied to different volcanoes or volcanic regions. Further, a similar strategy could be used to assess hazards associated with other volcanic phenomena such as lahars or tephra fall.

Appendix A: Statistics of Expected PDC Volume

Figure A1 shows the volumes observed in the Mono-Inyo PDC deposits. Data are collected from Bursik et al. (2014), Miller (1985), and Sieh and Bursik (1986). There are 11 volume estimates, ranging from 0.005 to 0.06 km^3 and including both BAF generated by lava dome collapse (e.g., Panum BAF) and pumice flows from eruptive column collapse (e.g., Panum Dune flow). We rely on information on the three most recent eruptions that occurred in the LVVR: the Inyo eruption (South Deadman flow of 0.05 km^3 and half of Obsidian flow pyroclastic deposits of 0.01 km^3), North Mono eruption (Panum Dune flow of 0.009 km^3, Panum BAF of 0.033 km^3, Panum Uppermost flow of 0.017 km^3, West flow of 0.05 km^3, and undifferentiated flows of 0.019 km^3), and South Mono eruption (half of Upper Gray beds of 0.06 km^3, half of Orange Brown beds of 0.02 km^3, and half of the Basal beds of 0.005 km^3). The first two of these eruptions occurred in 1338 CE ±13

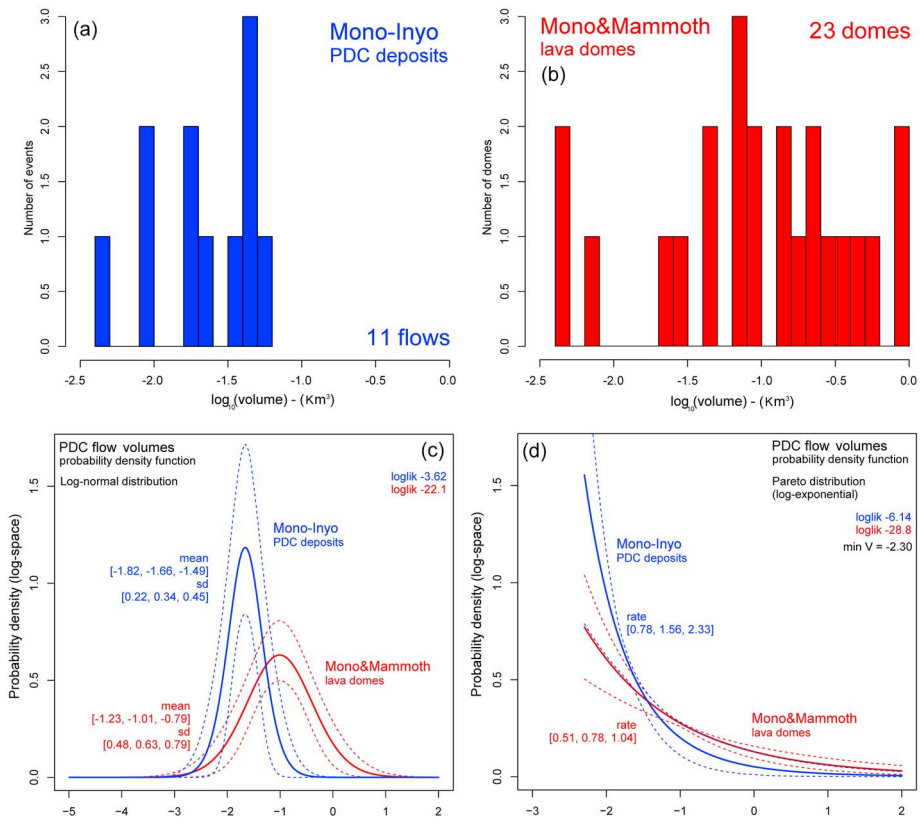

Figure A1. (a, b) Histograms of the volume of Mono-Inyo PDC deposits (blue) and lava domes (red). (c, d) Maximum likelihood pdf of the volume. (c) Assumes lognormal and (d) Pareto distribution. Dashed lines show the 90% symmetric confidence for the values of the pdf. Labels report the parameter values with 90% confidence interval.
PDC = pyroclastic density current.

separated by a ~1- to 2-year gap, while the third eruption occurred in 621 CE ±13. We also include Wilson Butte flow, of 0.04 km^3, and occurred in 290 CE ±50. Volumes below 0.001 km^3 is missing in our data set. Often, small deposits may not be preserved as they are prone to wash away or because of the difficulty to distinguish among the ash layers. A table summary of these values is included in the supporting information. Because of their sparsity, these data represent a preliminary approximation to the real volume distribution of past flows.

Given the local complex intercalation of fall, flow, and surge deposits, making it difficult to trace distinct beds, we applied a multiplicative corrector of 0.5 to the total volume published for the South Mono eruption flows and the Obsidian flow pyroclastic flows. Volumes below 0.001 km^3 are missing in our data set. Deposits of such small volumes may not be well preserved as they are prone to erosion and redeposition, and they are underrecorded because we have not separated them out for the South Deadman and South Mono flow deposits. The average value of measured Mono-Inyo PDC deposits is well represented by a value of $v \approx 0.03$ km^3. Again, some of the PDC deposits are known to be a combination of two or three separate, similar PDCs in rapid sequence (minutes to hours), difficult to distinguish, and possibly from multiple sources. For this reason, in Figure 8, we detailed the scenario of a single flow with $v = 0.01$ km^3.

Although the volume of domes and the volume of related PDCs are very uncertainly related, dome collapse is certainly an initiation mechanism for LVVR flows. Hence, we tentatively inferred additional flow volumes from lava dome volumes, including those of the Mammoth Mountain domes. Results are included in Figure A1 and are collected from Bevilacqua et al. (2018), Burkett (2007), Bursik et al. (2014), Miller (1985), and Sieh and Bursik (1986). Average dome volumes are about 1 order of magnitude larger than those obtained from measured PDC deposits. We applied a multiplicative corrector of 2.5 to pass from dense rock (DRE) to an equivalent pyroclastic volume. However, the resulting values may be overestimating those of

actual dome collapse flows because domes usually only collapse partially. There are thus 23 additional volume estimates, ranging from 0.006 to 0.96 km^3. We rely on dome and lava flow volumes for the Inyo eruption (Glass Creek dome of 0.25 km^3, Obsidian Flow dome of 0.43 km^3, and South Deadman dome of 0.33 km^3), the North Mono eruption (Cratered Dome of 0.005 km^3, Panum Dome of 0.03 km^3, Panum tephra ring of 0.007 km^3, North Coulee of 0.96 km^3, Upper Dome of 0.093 km^3, and Satellite Dome of 0.005 km^3), the South Mono eruption (South Coulee 0.81 km^3), and Wilson Butte eruption (Wilson Butte of 0.13 km^3), and 12 of the domes of the Mammoth Mountain dome complex approximately erupted from 100 to 50 ka and ranging from 0.025 to 0.58 km^3 in volume. These values are also summarized in the supporting information.

The average value of tephra equivalent to the rock volume of measured domes is well represented by $v \approx 0.2$ km^3. However, in Figure 4, we detailed the scenario of a single flow with $v = 1$ km^3, related to the total collapse of the largest domes and flows in the record (North Coulee and South Coulee). We remark that such an extremely large event is not assumed to be likely in the LVVR but is consistent with the largest scale of the effusive phases of the most recent events. The chance of events more extreme in volume than the PDCs observed in the past is subject to great uncertainty and strongly depends on the statistical model adopted for the extrapolation of the tail of the probability distribution of the PDC volumes reported in Figure A1. For example, assuming a lognormal distribution, the 95th percentile of the volume is $v \approx 0.1$ km^3, but if the Pareto distribution is assumed, this value increases to $v \approx 1$ or 2 km^3. The 95th percentile values obtained from the lava domes are 2 orders of magnitude larger than these values. However, lava domes of such sizes ($\gg$1 km) are almost completely unknown in the geologic record and certainly unknown at LVVR. In general, the logarithm of the observed volumes is compatible with the null hypothesis of the Shapiro-Wilk test for a Gaussian distribution, and the maximum likelihood in the lognormal class is significantly higher than in the Pareto class (see Figure A1).

Acknowledgments
The research was supported by the NSF under Grants DMS-1228317-1228265-1228217, EAR-1331353, DMS-1622403-1621853-1622467, DMS-1638521, DMS-1821311-1821338-1821289, OAC-1339765, and SES-1521855. This research was also supported by the Italian Ministry of Education, University, and Research, project FISR2017-SOIR. Data for vent opening maps are posted and freely available on VHUB online (https://vhub.org/resources/4518https://vhub.org/resources/4518) as is data for maps corresponding to Figures 4a–4c, 55c, and 88a–8c in this paper at their website (https://vhub.org/resources/4579https://vhub.org/resources/4579).

References

Achauer, U., Greene, L., Evans, J. R., & Iyer, H. (1986). Nature of the magma chamber underlying the Mono Craters area, eastern California, as determined from teleseismic travel time residuals. *Journal of Geophysical Research*, *91*, 13,873–13,891.

Aspinall, W., Woo, G., Voight, B., & Baxter, P. (2003). Evidence-based volcanology: Application to eruption crises. *Journal of Volcanology and Geothermal Research*, *128*(1), 273–285. https://doi.org/10.1016/S0377-0273(03)00260-9

Bailey, R. A. (1989). Geologic map of Long Valley Caldera. *Mono-Inyo craters volcanic chain, and vicinity, eastern California: US geological survey miscellaneous investigations map I-1933, scale*, *1*(62,500), 11.

Bailey, R. A. (2004). Eruptive history and chemical evolution of the precaldera and postcaldera basalt-dacite sequences, Long Valley, California: Implications for magma sources, current seismic unrest, and future volcanism, US Department of the Interior.

Bailey, R. A., Dalrymple, G. B., & Lanphere, M. A. (1976). Volcanism, structure, and geochronology of Long Valley Caldera, Mono County, California. *Journal of Geophysical Research*, *81*, 725–744.

Bartolini, S., Cappello, A., Martí, J., & Del Negro, C. (2013). QVAST: A new quantum GIS plugin for estimating volcanic susceptibility. *Natural Hazards and Earth System Sciences*, *13*(11), 3031–3042. https://doi.org/10.5194/nhess-13-3031-2013

Bayarri, M. J., Berger, J. O., Calder, E. S., Dalbey, K., Lunagomez, S., Patra, A. K., et al. (2009). Using statistical and computer models to quantify volcanic hazards. *Technometrics*, *51*(4), 402–413. https://doi.org/10.1198/TECH.2009.08018

Bayarri, M. J., Berger, J. O., Calder, E. S., Patra, A. K., Pitman, E. B., Spiller, E. T., & Wolpert, R. L. (2015). A methodology for quantifying volcanic hazards. *International Journal for Uncertainty Quantification*, *5*(4), 297–325.

Bebbington, M. S. (2013). Assessing spatio-temporal eruption forecasts in a monogenetic volcanic field. *Journal of Volcanology and Geothermal Research*, *252*(Supplement C), 14–28. https://doi.org/10.1016/j.jvolgeores.2012.11.010

Bebbington, M. S. (2015). Spatio-volumetric hazard estimation in the Auckland volcanic field. *Bulletin of Volcanology*, *77*(5), 39. https://doi.org/10.1007/s00445-015-0921-3

Bebbington, M. S., & Cronin, S. J. (2011). Spatio-temporal hazard estimation in the Auckland Volcanic Field, New Zealand, with a new event-order model. *Bulletin of Volcanology*, *73*(1), 55–72. https://doi.org/10.1007/s00445-010-0403-6

Bergfeld, D., Evans, W. C., Howle, J. F., & Hunt, A. G. (2015). Magmatic gas emissions at Holocene volcanic features near Mono Lake, California, and their relation to regional magmatism. *Journal of Volcanology and Geothermal Research*, *292*, 70–83.

Bevilacqua, A., Bursik, M., Patra, A., Bruce Pitman, E., Yang, Q., Sangani, R., & Kobs-Nawotniak, S. (2018). Late quaternary eruption record and probability of future volcanic eruptions in the Long Valley Volcanic Region (CA, USA). *Journal of Geophysical Research: Solid Earth*, *123*, 5466–5494. https://doi.org/10.1029/2018JB015644

Bevilacqua, A., Bursik, M., Patra, A., Pitman, E. B., & Till, R. (2017). Bayesian construction of a long-term vent opening map in the Long Valley volcanic region, (CA, USA). *Statistics in Volcanology*, *3*(1), 1–36. https://doi.org/10.5038/2163-338X.3.1

Bevilacqua, A., Bursik, M. I., Patra, A., Pitman, E. B., & Till, R. (2019). Vent opening maps dataset for Long Valley volcanic region.

Bevilacqua, A., Flandoli, F., Neri, A., Isaia, R., & Vitale, S. (2016). Temporal models for the episodic volcanism of Campi Flegrei caldera (Italy) with uncertainty quantification. *Journal of Geophysical Research: Solid Earth*, *121*, 7821–7845. https://doi.org/10.1002/2016JB013171

Bevilacqua, A., Isaia, R., Neri, A., Vitale, S., Aspinall, W. P., Bisson, M., et al. (2015). Quantifying volcanic hazard at Campi Flegrei caldera (Italy) with uncertainty assessment: 1. Vent opening maps. *Journal of Geophysical Research: Solid Earth*, *120*, 2309–2329. https://doi.org/10.1002/2014JB011775

Bevilacqua, A., Neri, A., Bisson, M., Esposti Ongaro, T., Flandoli, F., Isaia, R., et al. (2017). The effects of vent location, event scale, and time forecasts on pyroclastic density current hazard maps at Campi Flegrei caldera (Italy). *Frontiers in Earth Science*, *5*, 72. https://doi.org/10.3389/feart.2017.00072

Bevilacqua, A., Patra, A. K., Bursik, M. I., Pitman, E. B., Macías, J. L., Saucedo, R., & Hyman, D. (2019). Probabilistic forecasting of plausible debris flows from Nevado de Colima (Mexico) using data from the Atenquique debris flow, 1955. *Natural Hazards and Earth System Sciences*, *19*(4), 791–820.

Biass, S., Bonadonna, C., Connor, L., & Connor, C. (2016). Tephraprob: A matlab package for probabilistic hazard assessments of tephra fallout. *Journal of Applied Volcanology*, *5*(10), 1–16.

Biass, S., Bonadonna, C., Di Traglia, F., Pistolesi, M., Rosi, M., & Lestuzzi, P. (2016). Probabilistic evaluation of the physical impact of future tephra fallout events for the island of Vulcano, Italy. *Bulletin of Volcanology*, *78*(5), 1. https://doi.org/10.1186/s13617-016-0050-5

Bucklew, J. (2010). *Introduction to rare event simulation introduction to rare event simulation* (1st). New York: Springer Publishing Company, Incorporated.

Burkett, S. M. (2007). Geomorphic mapping and petrography of Mammoth Mountain, California.

Bursik, M., Patra, A., Pitman, E., Nichita, C., Macias, J., Saucedo, R., & Girina, O. (2005). Advances in studies of dense volcanic granular flows. *Reports on Progress in Physics*, *68*(2), 271.

Bursik, M., Sieh, K., & Meltzner, A. (2014). Deposits of the most recent eruption in the Southern Mono Craters, California: Description, interpretation and implications for regional marker tephras. *Journal of Volcanology and Geothermal Research*, *275*, 114–131.

Cappello, A., Geshi, N., Neri, M., & Negro, C. D. (2015). Lava flow hazards—An impending threat at Miyakejima Volcano, Japan. *Journal of Volcanology and Geothermal Research*, *308*(Supplement C), 1–9. https://doi.org/10.1016/j.jvolgeores.2015.10.005

Capra, L., Manea, V., Manea, M., & Norini, G. (2011). The importance of digital elevation model resolution on granular flow simulations: A test case for Colima volcano using TITAN2D computational routine. *Natural Hazards*, *59*(2), 665–680. https://doi.org/10.1007/s11069-011-9788-6

Carey, S., Sigurdsson, H., Mandeville, C., & Bronto, S. (1996). Pyroclastic flows and surges over water: An example from the 1883 Krakatau eruption. *Bulletin of Volcanology*, *57*(7), 493–511.

Chapman, N., Apted, M., Aspinall, W. P., Berryman, K., Cloos, M., Connor, C. B., et al. (2012). Topaz project: Long-term tectonic hazard to geological repositories. *Nuclear Waste Management Organization of Japan (NUMO) Report*, 1–87.

Charbonnier, S. J., & Gertisser, R. (2009). Numerical simulations of block-and-ash flows using the TITAN2D flow model: Examples from the 2006 eruption of Merapi Volcano, Java, Indonesia. *Bulletin of Volcanology*, *71*(8), 953–959.

Charbonnier, S. J., & Gertisser, R. (2012). Evaluation of geophysical mass flow models using the 2006 block-and-ash flows of Merapi Volcano, Java, Indonesia: Towards a short-term hazard assessment tool. *Journal of Volcanology and Geothermal Research*, *231*, 87–108.

Connor, L. J., Connor, C. B., Meliksetian, K., & Savov, I. (2012). Probabilistic approach to modeling lava flow inundation: A lava flow hazard assessment for a nuclear facility in Armenia. *Journal of Applied Volcanology*, *1*(1), 3. https://doi.org/10.1186/2191-5040-1-3

Connor, C. B., & Hill, B. E. (1995). Three nonhomogeneous poisson models for the probability of basaltic volcanism: Application to the Yucca Mountain Region, Nevada. *Journal of Geophysical Research*, *100*, 10,107–10,125. https://doi.org/10.1029/95JB01055

Connor, C. B., Stamatakos, J. A., Ferrill, D. A., Hill, B. E., Ofoegbu, G. I., Conway, F. M., et al. (2000). Geologic factors controlling patterns of small-volume basaltic volcanism: Application to a volcanic hazards assessment at Yucca Mountain, Nevada. *Journal of Geophysical Research*, *105*, 417–432. https://doi.org/10.1029/1999JB900353

Cox, D. R., & Isham, V. (1980). *Point processes*. Boca Raton, New York, London, Washington, DC: Chapman and Hall/CRC Press.

Dalbey, K., Patra, A., Pitman, E., Bursik, M., & Sheridan, M. (2008). Input uncertainty propagation methods and hazard mapping of geophysical mass flows. *Journal of Geophysical Research*, *113*, B05203. https://doi.org/10.1029/2006JB004471

Dennen, R., Bursik, M., & Roche, O. (2014). Dome collapse mechanisms and block-and-ash flow emplacement dynamics inferred from deposit and impact mark analysis, Mono Craters, CA. *Journal of Volcanology and Geothermal Research*, *276*, 1–9.

Edmonds, M., & Herd, R. A. (2005). Inland-directed base surge generated by the explosive interaction of pyroclastic flows and seawater at Soufriere Hills volcano, Montserrat. *Geology*, *33*(4), 245–248.

Farrar, C., Sorey, M., Evans, W. C., Howle, J., Kerr, B., Kennedy, B. M., et al. (1995). Forest-killing diffuse CO_2 emission at Mammoth Mountain as a sign of magmatic unrest. *Nature*, *376*(6542), 675–678.

Flinders, A. F., Shelly, D. R., Dawson, P. B., Hill, D. P., Tripoli, B., & Shen, Y. (2018). Seismic evidence for significant melt beneath the Long Valley Caldera, California, USA. *Geology*, *46*(9), 799. https://doi.org/10.1130/G45094.1

Foulger, G. R., Julian, B. R., Pitt, A. M., Hill, D. P., Malin, P. E., & Shalev, E. (2003). Three-dimensional crustal structure of Long Valley Caldera, California, and evidence for the migration of CO_2 under Mammoth Mountain. *Journal of Geophysical Research*, *108*(B3), 2147. https://doi.org/10.1029/2000JB000041

Gallant, E., Richardson, J., Connor, C., Wetmore, P., & Connor, L. (2018). A new approach to probabilistic lava flow hazard assessments, applied to the Idaho National Laboratory, Eastern Snake River Plain, Idaho, USA. *Geology*, *46*(10), 895. https://doi.org/10.1130/G45123.1

Gerlach, T. M., Doukas, M. P., McGee, K. A., & Kessler, R. (1998). Three-year decline of magmatic CO_2 emissions from soils of a Mammoth Mountain tree kill: Horseshoe Lake, CA, 1995–1997. *Geophysical Research Letters*, *25*, 1947–1950.

Gerlach, T. M., Doukas, M. P., McGee, K. A., & Kessler, R. (1999). Airborne detection of diffuse carbon dioxide emissions at Mammoth Mountain, California. *Geophysical Research Letters*, *26*, 3661–3664.

Gu, M., & Berger, J. O. (2016). Parallel partial Gaussian process emulation for computer models with massive output. *The Annals of Applied Statistics*, *10*(3), 1317–1347.

Hayashi, J., & Self, S. (1992). A comparison of pyroclastic flow and debris avalanche mobility. *Journal of Geophysical Research*, *97*, 9063–9071.

Hildreth, W. (2004). Volcanological perspectives on Long Valley, Mammoth Mountain, and Mono Craters: Several contiguous but discrete systems. *Journal of Volcanology and Geothermal Research*, *136*(3), 169–198.

Hildreth, W. (2017). Fluid-driven uplift at Long Valley Caldera, California: Geologic perspectives. *Journal of Volcanology and Geothermal Research*, *341*, 269–286.

Hildreth, W., & Fierstein, J. (2016). Eruptive history of mammoth mountain and its mafic periphery, California (Tech. Rep.): US Geological Survey.

Hildreth, W., Fierstein, J., & Calvert, A. (2017). Early postcaldera rhyolite and structural resurgence at Long Valley Caldera, California. *Journal of Volcanology and Geothermal Research*, *335*, 1–34.

Hildreth, W., Fierstein, J., Champion, D., & Calvert, A. (2014). Mammoth mountain and its mafic periphery? A late Quaternary volcanic field in eastern California. *Geosphere*, *10*(6), 1315–1365.

Hildreth, W., & Mahood, G. A. (1986). Ring-fracture eruption of the bishop tuff. *Geological Society of America Bulletin*, *97*(4), 396–403.

Hill, D. P. (2006). Unrest in Long Valley Caldera, California, 1978–2004. *Geological Society, London, Special Publications*, *269*(1), 1–24.

Hill, D. P., Mangan, M. T., & McNutt, S. R. (2017). Volcanic region, California volcanic unrest and hazard communication in Long Valley volcanic region, California.

Iverson, R. (1997). The physics of debris flows. *Reviews of Geophysics*, *35*(3), 245–296.

Iverson, R. M., & Denlinger, R. P. (2001). Flow of variably fluidized granular masses across three-dimensional terrain: 1. Coulomb mixture theory. *Journal of Geophysical Research*, *106*, 537–552.

Iverson, R. M., & George, D. L. (2014). A depth-averaged debris-flow model that includes the effects of evolving dilatancy. I. Physical basis. *Proceedings of the Royal Society of London A: Mathematical, Physical and Engineering Sciences*, *470*, 2170. https://doi.org/10.1098/rspa.2013.0819

Jaquet, O., Lantuéjoul, C., & Goto, J. (2012). Probabilistic estimation of long-term volcanic hazard with assimilation of geophysics and tectonic data. *Journal of Volcanology and Geothermal Research*, *235-236*(Supplement C), 29–36. https://doi.org/10.1016/j.jvolgeores.2012.05.003

Jaquet, O., Lantuéjoul, C., & Goto, J. (2017). Probabilistic estimation of long-term volcanic hazard under evolving tectonic conditions in a 1 Ma timeframe. *Journal of Volcanology and Geothermal Research*, *345*(Supplement C), 58–66. https://doi.org/10.1016/j.jvolgeores.2017.07.010

Johnson, M. E., Moore, L. M., & Ylvisaker, D. (1990). Minimax and maximin distance designs. *Journal of statistical planning and inference*, *26*(2), 131–148.

Kaye, G., Cole, J., King, A., & Johnston, D. (2009). Comparison of risk from pyroclastic density current hazards to critical infrastructure in Mammoth Lakes, California, USA, from a new Inyo craters rhyolite dike eruption versus a dacitic dome eruption on Mammoth Mountain. *Natural Hazards*, *49*(3), 541–563. https://doi.org/10.1007/s11069-008-9313-8

Magill, C. R., McAneney, K. J., & Smith, I. E. M. (2005). Probabilistic assessment of vent locations for the next Auckland volcanic field event. *Mathematical Geology*, *37*(3), 227–242. https://doi.org/10.1007/s11004-005-1556-2

Mahood, G. A., Ring, J. H., Manganelli, S., & McWilliams, M. O. (2010). New $^{40}AR/^{39}AR$ ages reveal contemporaneous mafic and silicic eruptions during the past 160,000 years at Mammoth Mountain and Long Valley Caldera, California. *Geological Society of America Bulletin*, *122*(3-4), 396–407.

Mandeville, C. W., Carey, S., & Sigurdsson, H. (1996). Magma mixing, fractional crystallization and volatile degassing during the 1883 eruption of Krakatau Volcano, Indonesia. *Journal of Volcanology and Geothermal Research*, *74*(3-4), 243–274.

Marti, J., & Felpeto, A. (2010). Methodology for the computation of volcanic susceptibility: An example for mafic and felsic eruptions on Tenerife (Canary Islands). *Journal of Volcanology and Geothermal Research*, *195*(1), 69–77. https://doi.org/10.1016/j.jvolgeores.2010.06.008

Martin, A. J., Umeda, K., Connor, C. B., Weller, J. N., Zhao, D., & Takahashi, M. (2004). Modeling long-term volcanic hazards through Bayesian inference: An example from the Tohoku Volcanic Arc, Japan. *Journal of Geophysical Research*, *109*, B10208. https://doi.org/10.1029/2004JB003201

Marzocchi, W., & Bebbington, M. S. (2012). Probabilistic eruption forecasting at short and long time scales. *Bulletin of Volcanology*, *74*(8), 1777–1805. https://doi.org/10.1007/s00445-012-0633-x

Marzocchi, W., Sandri, L., Gasparini, P., Newhall, C., & Boschi, E. (2004). Quantifying probabilities of volcanic events: The example of volcanic hazard at Mount Vesuvius. *Journal of Geophysical Research*, *109*, B11201. https://doi.org/10.1029/2004JB003155

Marzocchi, W., Sandri, L., & Selva, J. (2010). BET_VH: A probabilistic tool for long-term volcanic hazard assessment. *Bulletin of Volcanology*, *72*(6), 705–716. https://doi.org/10.1007/s00445-010-0357-8

Mastin, L. G., Van Eaton, A. R., & Lowenstern, J. B. (2014). Modeling ash fall distribution from a Yellowstone supereruption. *Geochemistry, Geophysics, Geosystems*, *15*, 3459–3475. https://doi.org/10.1002/2014gc005469

Mazzarini, F., Keir, D., & Isola, I. (2013). Spatial relationship between earthquakes and volcanic vents in the central-northern Main Ethiopian Rift. *Journal of Volcanology and Geothermal Research*, *262*(Supplement C), 123–133. https://doi.org/10.1016/j.jvolgeores.2013.05.007

Mazzarini, F., Le Corvec, N., Isola, I., & Favalli, M. (2016). Volcanic field elongation, vent distribution, and tectonic evolution of a continental rift: The Main Ethiopian Rift example. *Geosphere*, *12*(3), 706. https://doi.org/10.1130/GES01193.1

Mead, S. R., & Magill, C. R. (2017). Probabilistic hazard modelling of rain-trigged lahars. *Journal of Applied Volcanology*, *6:8*, 1–7. https://doi.org/10.1186/s13617-017-0060-y

Miller, C. D. (1985). Holocene eruptions at the Inyo volcanic chain, California: Implications for possible eruptions in Long Valley Caldera. *Geology*, *13*(1), 14–17.

Miller, C. D., Mullineaux, D., Crandell, D. R., & Bailey, R. (1982). Potential hazards from future volcanic eruptions in the Long Valley-Mono Lake area, east-central California and southwest Nevada: A preliminary assessment (Tech. Rep.): United States Dept. of the Interior, Geological Survey.

Montgomery-Brown, E., Wicks, C., Cervelli, P. F., Langbein, J. O., Svarc, J. L., Shelly, D. R., et al. (2015). Renewed inflation of Long Valley Caldera, California (2011 to 2014). *Geophysical Research Letters*, *42*, 5250–5257. https://doi.org/10.1002/2015gl064338

Neri, A., Bevilacqua, A., Esposti Ongaro, T., Isaia, R., Aspinall, W. P., Bisson, M., et al. (2015). Quantifying volcanic hazard at Campi Flegrei caldera (Italy) with uncertainty assessment: 2. Pyroclastic density current invasion maps. *Journal of Geophysical Research: Solid Earth*, *120*, 2330–2349. https://doi.org/10.1002/2014JB011776

Neri, A., Esposti Ongaro, T., Macedonio, G., & Gidaspow, D. (2003). Multiparticle simulation of collapsing volcanic columns and pyroclastic flow. *Journal of Geophysical Research*, *108*(B4), 2202. https://doi.org/10.1029/2001JB000508

Ogata, Y., & Akaike, H. (1982). On linear intensity models for mixed doubly stochastic poisson and self-exciting point processes. *Journal of the Royal Statistical Society. Series B (Methodological)*, *44*(1), 102–107.

Ogburn, S. E. (2014). *Reconciling field observations of pyroclastic density currents with conceptual and computational analogs using a GIS and a newly developed global database*. Buffalo, NY: State University of New York at Buffalo.

Ogburn, S. E., Berger, J. O., Calder, E. S., Lopes, D., Patra, A., Pitman, E. B., et al. (2016). Pooling strength amongst limited datasets using hierarchical Bayesian analysis, with application to pyroclastic density current mobility metrics. *Statistics in Volcanology*, *2*(1), 1.

Ogburn, S. E., & Calder, E. S. (2017). The relative effectiveness of empirical and physical models for simulating the dense undercurrent of pyroclastic flows under different emplacement conditions. *Frontiers in Earth Science*, *5*, 83.

Ogburn, S. E., Calder, E. S., Cole, P. D., & Stinton, A. J. (2014). The effect of topography on ash-cloud surge generation and propagation. *Geological Society, London, Memoirs*, *39*(1), 179–194.

Papoulis, A., & Pillai, S. U. (2002). *Probability, random variables, and stochastic processes*. Boston: McGraw Hill.

Patra, A., Bauer, A., Nichita, C., Pitman, E., Sheridan, M., & Bursik, M. (2005). Parallel adaptive numerical simulation of dry avalanches over natural terrain. *Journal of Volcanology and Geothermal Research*, *139*(1–2), 1–21. https://doi.org/10.1016/j.jvolgeores.2004.06.014

Peacock, J. R., Mangan, M. T., McPhee, D., & Ponce, D. A. (2015). Imaging the magmatic system of Mono Basin, California, with magnetotellurics in three dimensions. *Journal of Geophysical Research: Solid Earth*, *120*, 7273–7289. https://doi.org/10.1002/2015jb012071

Peacock, J. R., Mangan, M. T., McPhee, D., & Wannamaker, P. E. (2016). Three-dimensional electrical resistivity model of the hydrothermal system in Long Valley Caldera, California, from magnetotellurics. *Geophysical Research Letters*, *43*, 7953–7962. https://doi.org/10.1002/2016GL069263

Pitman, E. B., & Le, L. (2005). A two-fluid model for avalanche and debris flows. *Philosophical Transactions. Series A, Mathematical, Physical, and Engineering Sciences*, *363*(1832), 1573–601. https://doi.org/10.1098/rsta.2005.1596

Pitman, E. B., Nichita, C. C., Patra, A. K., Bauer, A., Sheridan, M. F., & Bursik, M. (2003). Computing granular avalanches and landslides computing granular avalanches and landslides. *Physics of Fluids*, *15*(12), 3638–3646.

Prejean, S. G. (2003). The interaction of tectonic and magmatic processes in the Long Valley Caldera, California (Unpublished doctoral dissertation), Stanford University.

Rasmussen, C., & Williams, C. (2006). *Gaussian processes for machine learning Gaussian processes for machine learning*. Cambridge, MA, London, England: University Press Group Limited.

Ross, S. (2012). *Simulation simulation*. San Diego, Boston, London, Amsterdam: Elsevier Science.

Sacks, J., Schiller, S., & Welch, W. (1989). Designs for computer experiments. *Technometrics*, *31*(1), 41–47.

Sandri, L., Costa, A., Selva, J., Tonini, R., Macedonio, G., Folch, A., & Sulpizio, R. (2016). Beyond eruptive scenarios: Assessing tephra fallout hazard from Neapolitan volcanoes. *Nature, Scientific Reports*, *6*(24271). https://doi.org/10.1038/srep24271

Sandri, L., Jolly, G., Lindsay, J., Howe, T., & Marzocchi, W. (2012). Combining long- and short-term probabilistic volcanic hazard assessment with cost-benefit analysis to support decision making in a volcanic crisis from the Auckland volcanic field, New Zealand. *Bulletin of Volcanology*, *74*(3), 705–723. https://doi.org/10.1007/s00445-011-0556-y

Sandri, L., Tierz, P., Costa, A., & Marzocchi, W. (2018). Probabilistic hazard from pyroclastic density currents in the Neapolitan area (southern Italy). *Journal of Geophysical Research: Solid Earth*, *123*, 3474–3500. https://doi.org/10.1002/2017jb014890

Santner, T. J., Williams, B. J., & Notz, W. I. (2013). *The design and analysis of computer experiments*. New York: Springer Science & Business Media.

Savage, S., & Hutter, K. (1989). The motion of a finite mass of granular material down a rough incline. *Journal of Fluid Mechanics*, *199*, 177–215. https://doi.org/10.1017/S0022112089000340

Selva, J., Costa, A., Marzocchi, W., & Sandri, L. (2010). Bet_vh: exploring the influence of natural uncertainties on long-term hazard from tephra fallout at Campi Flegrei (Italy). *Bulletin of Volcanology*, *72*(6), 717–733. https://doi.org/10.1007/s00445-010-0358-7

Selva, J., Costa, A., Sandri, L., Macedonio, G., & Marzocchi, W. (2014). Probabilistic short-term volcanic hazard in phases of unrest: A case study for tephra fallout. *Journal of Geophysical Research: Solid Earth*, *119*, 8805–8826. https://doi.org/10.1002/2014JB011252

Selva, J., Orsi, G., Di Vito, M. A., Marzocchi, W., & Sandri, L. (2012). Probability hazard map for future vent opening at the Campi Flegrei caldera, Italy. *Bulletin of Volcanology*, *74*(2), 497–510. https://doi.org/10.1007/s00445-011-0528-2

Shelly, D. R., & Hill, D. P. (2011). Migrating swarms of brittle-failure earthquakes in the lower crust beneath Mammoth Mountain, California. *Geophysical Research Letters*, *38*, L20307. https://doi.org/10.1029/2011GL049336

Shelly, D. R., Taira, T., Prejean, S. G., Hill, D. P., & Dreger, D. S. (2015). Fluid-faulting interactions: Fracture-mesh and fault-valve behavior in the February 2014 Mammoth Mountain, California, earthquake swarm. *Geophysical Research Letters*, *42*, 5803–5812. https://doi.org/10.1002/2015gl064325

Sheridan, M. F. (1979). Emplacement of pyroclastic flows: A review. *Geological Society of America Special Paper*, *180*, 125–136.

Sieh, K., & Bursik, M. (1986). Most recent eruption of the Mono Craters, eastern central California. *Journal of Geophysical Research*, *91*, 12,539–12,571.

Sigurdsson, H., & Carey, S. (1989). Plinian and co-ignimbrite tephra fall from the. *Bulletin of Volcanology*, *51*(4), 243–270.

Sobradelo, R., & Marti, J. (2010). Bayesian event tree for long-term volcanic hazard assessment: Application to Teide-Pico Viejo stratovolcanoes, Tenerife, Canary Islands. *Journal of Geophysical Research*, *115*, B05206. https://doi.org/10.1029/2009JB006566

Sobradelo, R., & Marti, J. (2015). Short-term volcanic hazard assessment through Bayesian inference: Retrospective application to the Pinatubo 1991 volcanic crisis. *Journal of Volcanology and Geothermal Research*, *290*(Supplement C), 1–11. https://doi.org/10.1016/j.jvolgeores.2014.11.011

Sparks, R. S. J. (2003). Forecasting volcanic eruptions. *Earth and Planetary Science Letters*, *210*, 1–15.

Sparks, R. S. J., & Aspinall, W. P. (2013). Volcanic activity: Frontiers and challenges in forecasting, prediction and risk assessment. In *The state of the planet: Frontiers and challenges in geophysics* (pp. 359–373). Washington, DC: American Geophysical Union. https://doi.org/10.1029/150GM28

Spiller, E. T., Bayarri, M. J., Berger, J. O., Calder, E. S., Patra, A. K., Bruce, P. E., & Wolpert, R. L. (2014). Automating emulator construction for geophysical hazard maps. *SIAM/ASA Journal on Uncertainty Quantification*, *2*(1), 126–152.

Tadini, A., Bevilacqua, A., Neri, A., Cioni, R., Aspinall, W. P., Bisson, M., et al. (2017). Assessing future vent opening locations at the Somma-Vesuvio volcanic complex: 2. Probability maps of the caldera for a future Plinian/sub-Plinian event with uncertainty quantification. *Journal of Geophysical Research: Solid Earth*, *122*, 4357–4376. https://doi.org/10.1002/2016JB013860

Tierz, P., Stefanescu, E., Sandri, L., Sulpizio, R., Valentine, G., Marzocchi, W., & Patra, A. (2018). Towards quantitative volcanic risk of pyroclastic density currents: Probabilistic hazard curves and maps around Somma-Vesuvius (Italy). *Journal of Geophysical Research: Solid Earth*, *123*, 6299–6317. https://doi.org/10.1029/2017JB015383

TITAN2D Mass-Flow Simulation Tool (2010).

Valentine, G. A., & Sweeney, M. R. (2018). Compressible flow phenomena at inception of lateral density currents fed by collapsing gas-particle mixtures. *Journal of Geophysical Research: Solid Earth*, *123*, 1286–1302. https://doi.org/10.1002/2017JB015129

Valentine, G. A., & Wohletz, K. H. (1989). Numerical models of Plinian eruption columns and pyroclastic flows. *Journal of Geophysical Research*, *94*, 1867–1887. https://doi.org/10.1029/JB094iB02p01867

Volentik, A. C. M., & Houghton, B. F. (2015). Tephra fallout hazards at quito international airport (ecuador). *Bulletin of Volcanology*, *77*(6), 50. https://doi.org/10.1007/s00445-015-0923-1

Welch, W. J., Buck, R. J., Sacks, J., Wynn, H. P., Mitchell, T. J., & Morris, M. D. (1992). Screening, predicting, and computer experiments. *Technometrics*, *34*(1), 15–25.

Wood, C. A. (1983). Continental rift jumps. *Tectonophysics*, *94*(1-4), 529–540.

Yang, Q., Bursik, M., & Pouget, S. (2019). Stratigraphic and sedimentologic framework for tephras in the Wilson Creek Formation, Mono Basin, California, USA. *Journal of Volcanology and Geothermal Research*, *374*, 197–225.